Characterizing stellar parameters from high-resolution spectra of main sequence cool stars. I. The G2V-K2V stars

Logithan Kulenthirarajah, Jean-François Donati, Gaitee Hussain, Julien Morin, France Allard

Monthly Notices
of the
ROYAL ASTRONOMICAL SOCIETY

MNRAS **487,** 1335–1362 (2019)
Advance Access publication 2019 May 17

doi:10.1093/mnras/stz1270

Characterizing stellar parameters from high-resolution spectra of main sequence cool stars. I. The G2V–K2V stars

Logithan Kulenthirarajah,[1,2]★ Jean-François Donati,[1,2,3]★ Gaitee Hussain,[4] Julien Morin[5] and France Allard[6]

[1]*Institut de Recherche en Astrophysique et Planétologie (IRAP), Toulouse, France*
[2]*Université Paul Sabatier, Toulouse, France*
[3]*CNRS, Toulouse, France*
[4]*European Southern Observertory, Munich, Germany*
[5]*LUPM, Université de Montpellier, CNRS, Place Eugène Bataillon, F-34095 Montpellier, France*
[6]*CRAL, UMR 5574, CNRS, ENS, Université de Lyon, Lyon, France*

Accepted 2019 April 25. Received 2019 April 20; in original form 2018 November 25

ABSTRACT

The goal of the present study is to construct, test, and validate a high-resolution synthetic spectral library using PHOENIX model atmospheres and develop a reliable tool to estimate stellar parameters from high-resolution optical and/or near-infrared spectra of M dwarfs. We report here the preliminary results of tests characterizing main sequence G–K stars from high-resolution spectra. We anchored the atomic line-list using the stellar standards Sun, ξ Boo A, and ϵ Eri to ensure the synthetic spectra computed with PHOENIX reproduce their observed counterparts. These stars were chosen because their parameters are very well characterized, and on which the absolute accuracy of our method depends on.

We successfully estimated the stellar parameters with associated error bars for 17 stars. Using a pseudo Monte Carlo statistical analysis, we present overall improved uncertainties on the stellar parameters compared to those in the literature (on average 9 K, 0.014 dex, and 0.008 dex for the effective temperature, the surface gravity, and the metallicity, respectively). Our estimated stellar parameters are also in good agreement with values found in the literature.

Key words: stars: low-mass – stars: fundemental parameters.

1 INTRODUCTION

The determination of accurate stellar parameters is essential for constraining stellar evolution models which are necessary to understand stars and their evolution on the Hertzsprung–Russell (HR) diagram.

This paper describes the estimation of stellar parameters of G2V–K2V stars. It is the first step of a larger study to come that describes the characterization of stellar parameters starting from G to K-type stars with the aim of extending this analysis to M-type stars.

1.1 M dwarfs, the final objective

Parameters of M dwarfs can be estimated by comparing the flux ratio in different bands as a proxy of both effective temperature and metallicity (Casagrande, Flynn & Bessell 2008; Dressing & Charbonneau 2013; Gaidos et al. 2013; Neves et al. 2014). The radii can be estimated by interferometric measurements combined with photometry (Boyajian et al. 2012). Metallicities of M dwarfs can be reliably estimated (to a precision better than 0.1 dex) with improved calibration of existing methods (Mann et al. 2013a; Mann, Gaidos & Ansdell 2013b; Mann et al. 2014). Using empirically calibrated spectroscopic methods, the effective temperature can also be estimated (Santos et al. 2013; Mann et al. 2013b, 2015; Newton et al. 2015). Despite the considerable amount of work invested in successfully estimating the stellar parameters for M dwarfs using different methods (Rajpurohit et al. 2014, 2018a), none of them can reproduce the precision nor the consistency that can be achieved for F–G–K stars with a direct spectroscopic characterization (Brewer et al. 2015, 2016). M-dwarfs dominate the stellar population of our Galaxy, accounting for more than 75 per cent of all main sequence stars in the solar neighbourhood (Henry et al. 2006). This has a significant effect on various astrophysical problems, ranging from the study of stellar population, the study of exoplanets to Galactic evolution (Worthey 1994; Bruzual & Charlot 2003; Allard, Homeier & Freytag 2011; Baraffe et al. 2015a).

★ E-mail: lkulenthirar@irap.omp.eu (LK);
jean-francois.donati@irap.omp.eu (JFD)

Well-constrained stellar parameters are necessary to deduce properties of planets and their formation. Precise estimation of cool star parameters enables a new understanding of planet formation. M dwarfs have become the main targets for planet searches because of their smaller radii and lower masses compared to their solar counterparts. These two combined characteristics allow an easier detection of planets with transiting or radial velocity methods, particularly for planets in the insolation habitable zone (Dressing & Charbonneau 2015). Errors on the planet radii, radial velocity, and mass depend directly on the host star's parameters (Murihead et al. 2012; Dotter et al. 2008; Demory et al. 2009; Allard et al. 2011). A habitable zone is more complicated than a simple range of insolations. It highly depends on the effective temperature of the star. The lower the temperature, the redder the light. These wavelengths are more effective at heating, and so the habitable zone for red dwarf planets lies somewhat further out. Furthermore, studies based on the NASA Kepler mission suggest that there are at least 2.5 planets per M-dwarf (Bonfils et al. 2013; Dressing & Charbonneau 2015). Characterizing the M star planet population is therefore essential in any Galactic planet occurrence calculation. These numerous advantages motivate large planet surveys such as the near-infrared velocimeter CARMENES (Quirrenbach et al. 2012) and SPIRou (Donati et al. 2017) or future space-based telescope survey such as TESS (Ricker et al. 2014) and PLATO (Rauer et al. 2014). They are designed to detect hundreds of exoplanets, around M-dwarfs. It is imperative that we have accurate stellar parameters to fully exploit these data.

In studies involving Galactic structure and formation models, stellar abundance is a means of testing Galactic chemical evolution models, with the assumption being that the photospheric chemical composition of stars represents the local Galactic chemical composition where they formed. As the stellar mass function peaks around M stars, they have a significant impact in any study of Galactic structure, especially for constraining basic Milky Way formation models (Tinsley 1980). There is evidence that the ratio of low- to solar-metallicity M dwarfs is lower than predicted by Galactic evolution models; this is analogous to the five-decade long G-K stars problem (van den Bergh 1962; Schmidt 1963; Woolf & West 2012).

M dwarfs are also key objects to understand the generation of magnetic fields in cool stars (Morin et al. 2008). Since they span a wide range of masses – and hence internal structure – and rotation periods, they allow us to probe stellar dynamos operating far from the solar regime. In particular, as the lowest mass M dwarfs are fully convective (e.g. Baraffe et al. 2015b), their magnetism is thought to rely on non-solar dynamo processes questioning the role of the tachocline in the stellar dynamos (Morin 2012). Besides, recent rotation measurements of M dwarfs revealed the existence of a bimodal distribution of periods (Newton et al. 2016), which has to be understood as the result of the interplay between rotation, magnetic field generation and stellar winds. Progressing on these issues will require an accurate determination of stellar parameters along with magnetic properties and rotation periods for a large sample of M dwarfs.

If one wants to estimate with precision the parameters of M dwarfs using a new and/or different method, one needs to validate the aforementioned method and model used on on a spectral class with well-characterized spectra (e.g. G stars) and extend the estimation procedure step by step toward M dwarfs.

1.2 G dwarfs, the starting point

Stellar parameters for F–G–K stars can be directly estimated by comparing observations to a stellar spectral library with a reliable estimation tool (Valenti & Fischer 2005; Brewer et al. 2016). Valenti & Fischer (2005) uniformly analysed thousands of F–G–K stars using spectroscopic data to provide precise stellar parameters in their sample. Later, Torres et al. (2012) presented the limits of the previous analyses in terms of degeneracies between the surface gravity and the effective temperature. Brewer et al. (2015, 2016) recently corrected for these degeneracies by adding $\log g$ sensitive lines in the line-list and thus by expanding the cumulative line-list span for 170–390 Å for spectral windows spread over between 5000 and 8000 Å. There are already some limitations when it comes to F–G–K stars but this gets more difficult when we approach the M-star range as the presence of molecules complicates our understanding of their physical properties (Rajpurohit et al. 2018a,b).

Radiative transfer and stellar models can provide the means to analyse high-resolution spectra of stars in order to infer corresponding fundamental stellar parameters, but we are limited by molecular bands (these are poorly described or completely omitted), the completeness of the atomic and molecular line-lists, the lack of many high-resolution spectra as well as our comprehension of different line broadening parameters and numerical assumptions. However, these synthetic spectral libraries can provide spectra for a wide range of stellar parameters with complete control over both wavelength range and spectral resolution. The spectral transition from F to M stars requires model atmosphere codes that can treat both atomic and molecular lines accurately with the necessary micro-physics (heavier element formation, gravity settling, etc.). Such requirements cannot be met by existing standard model atmospheres such as Kurucz (Kurucz 1979). MARCS model atmosphere (Gustafsson et al. 2008) is able to address these problems, but we decided to use the PHOENIX model atmosphere code (Allard & Hauschildt 1995) to take advantage of an already existing collaboration with France Allard and her team. We want to construct, test, and validate a high-resolution synthetic spectral library using PHOENIX model atmospheres (Allard et al. 2011) with an accurate description of both molecular and atomic lines associated with a reliable tool to estimate stellar parameters of M dwarfs. Directly fitting observed high-resolution spectra to synthetic library can yield stellar parameters ($T_{\rm eff}$, $\log g$, and $\log [M/H]$), while simultaneously enabling us to conduct a systematic error analysis. This work is an essential step in the preparation of the scientific exploitation of the new high-resolution near-IR velocimeter and spectropolarimeter SPIRou (Donati et al. 2017) which has recently been installed on the Canada–France–Hawaii–Telescope (CFHT).

In this study, we present the first step of our calibration and validation of PHOENIX spectra for G–K stars, and we obtained $T_{\rm eff}$, $\log g$ and $\log [M/H]$ for 17 stars in this range of spectral types. We used empirical corrections on the line-list with the aim to constrain and improve on existing analyses. We also provide extended error analyses which demonstrate that we can have precise error bars and confront our predictions with literature values. In Section 2, we present the model atmosphere code, its settings, and the computation of synthetic spectra. We describe the estimation tool in Section 3. We compare the synthetic spectra to observations using our estimation tool and also analyse error bar estimates in Section 4. We compare our results to values in the published literature in Section 5 and finally we conclude in Section 6 with a brief summary of the study.

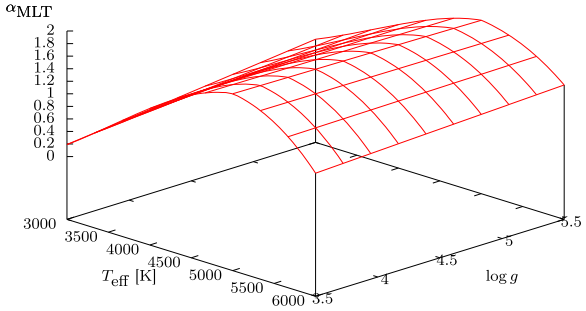

Figure 1. α_{MLT} from Ludwig et al. (1999) adapted for cool stars as a function of T_{eff} and log g.

2 SPECTRAL SYNTHESIS TOOL

2.1 Phoenix model atmosphere

PHOENIX is a state-of-the-art stellar and planetary atmosphere code that can compute atmospheres and spectra of stars across the HR-diagram, ranging from T Tauri and main sequence stars to evolved giants and white dwarfs, as well as for novae, supernovae, brown dwarfs, and extra-solar giant planets. This paper concentrates on low-mass stars (0.8 $M_{\odot} \leq M \leq 1.5\ M_{\odot}$) on the main sequence. The modelling of a stellar atmosphere is determined by three main parameters: the effective temperature (T_{eff}), the surface gravity (log g), and the global chemical composition relative to the Sun, i.e. the so-called metallicity (log [M/H]). Depending on these prior parameters, a simultaneous solution of the chemical equilibrium, the hydrostatic equilibrium, and radiative transfer equations is calculated iteratively until a prescribed criterion is reached. This provides the gas pressure, the local gas temperature, and the atmospheric density for different elements, what we call the atmosphere structure. A final radiative transfer iteration through the atmosphere structure will yield the synthetic spectra.

The energy transfer through radiation is described by the radiative transfer equations, and the convective energy transfer is described by the mixing length theory (Prandtl 1925; Böhm-Vitense 1958; Gough 1977). Both produce an energy flux through the atmosphere with energy conservation applied as no additional heat or radiation can be created inside the atmosphere. As the radiation is transported through absorption and re-emission by the gas, it is essential to have complete atomic and molecular line-lists. The MLT (mixing length theory) is defined by a characteristic non-dimensional length-scale $\alpha_{MLT} = l/L_H$, where l is the length-scale over which a blob of fluid will conserve its properties before mixing with the background fluid and L_H is the pressure scale height. We use α_{MLT} as a function of the effective temperature and the gravity to characterize convective motions in the lower part of the model atmosphere. It was previously calibrated by Ludwig, Freytag & Steffen (1999) for F to K stars using 3D radiative hydrodynamic simulations and later adapted for cooler stars (see Fig. 1) (Allard et al. 2011).

PHOENIX can account for effects of departures from local thermodynamic equilibrium (LTE) (H, He, Na, Mg, Ca, Ne, and Fe) and for anything else LTE is assumed. However, we set PHOENIX to compute in LTE for all species in order to save computation time during the validation process. PHOENIX computes models in 1D spherical mode with 128 layers using the latest BT-Settl model (Allard et al. 2011).

The PHOENIX model atmospheres are computed using one of many models already calculated by Allard et al. (2011) as initial conditions. From this computed model, we extended the grid step by step by making sure that the next model used the nearest newly computed model as a starting point in order to minimize the number of iterations required than if the same initial model was used each time. We iterated the stellar structure calculation until the convergence criterion is achieved. The convergence criterion is defined as the difference in per cent between the total flux per surface unit emitted and σT_{eff}^4 at each layer. Convergence is assumed when this criterion is lower than 3 per cent in radiative layers.

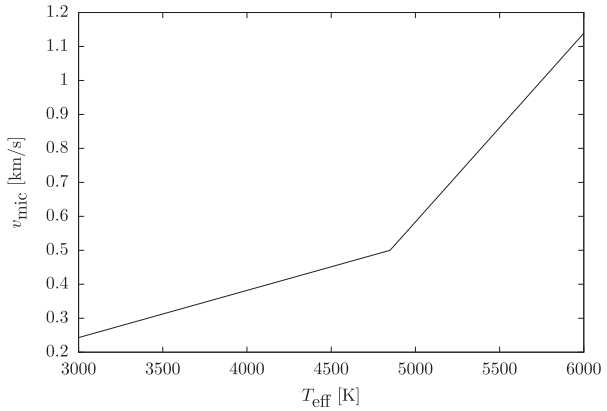

Figure 2. Microturbulence as a function of the effective temperature, as calibrated by Allard et al. (2011).

2.2 Phoenix synthetic spectra & continuum

Once the model structures were computed, PHOENIX was also used to produce fluxed spectra at high resolution. These 1D spectra were computed with adopted values for micro-turbulent and macro-turbulent velocity.

1D models consider a spherical symmetry which inherently assume that all the non-radial structures (starspots, granulation, magnetic fields) are negligible on average. Freytag et al. (2012) and Magic et al. (2013) have shown that 1D and 3D models can be significantly different. To correct for these differences, it is necessary to calibrate convection (MLT) or turbulence (micro/macro) related parameters on 3D simulations.

Allard et al. (2011) have conducted 2D RHD model atmosphere simulations to derive a relationship for the micro-turbulent motions as a function of T_{eff} for the BT–Settl model (see Fig. 2). Macro-turbulent motions do not affect the equivalent line width and thus can be applied a posteriori as Gaussian broadening (Takeda et al. 2007), whereas micro-turbulent motions directly affect line opacities (Gray 2005) and have to be included in the line formation process. Husser et al. (2013) proposed to use convective velocity, $\langle v_{conv} \rangle$, in the lower part of the radiative section of the atmosphere caused by overshooting at the interface between radiative and convective areas as a proxy for micro-turbulence. They suggested that large-scale motions directly affect the micro-turbulent motion based on 3D RHD simulations for M dwarfs (Wende, Reiners & Ludwig 2009). They also proposed to use $v_{micro} = 0.5\langle v_{conv} \rangle$ as a self-consistent way of measuring the micro-turbulence. We, on the other hand, used the calibration done by Allard et al. (2011) in 2D RHD with cloud simulations (see Fig. 2).

As most of the observed spectra are flux-normalized to the apparent continuum, it is necessary to have normalized synthetic spectra to compare against observed data. An improper placement of the continuum will lead to systematic errors in the parameter estimations and erroneous conclusions. As the entire purpose of

this paper is to minimize the aforementioned systematics, we have to be even more careful when identifying the continuum from the synthetic spectra. We used PHOENIX to compute the actual continuum for given stellar parameters. This is done by removing the discrete opacities, making any atomic and molecular data unavailable and by keeping dust and continuous opacities.This yields a close to perfect continuum placement on the synthetic spectra. The continuum was computed at a lower resolution than the spectrum and then interpolated to the full resolution to optimize computing time. The error introduced by interpolation of the continuum compared to the full resolution is negligible and does not introduce any systematics. Note that, for any stars cooler than late K-type stars, the molecular opacities start to dominate any continuous opacities by several orders of magnitude. This renders the positioning of the continuum more difficult (Allard & Hauschildt 1995).

3 SPECTROSCOPIC ANALYSIS

Directly comparing the observed and synthetic spectra across multiple spectral domains in wavelength enables us to model all observed spectra uniformly, regardless of external constraints. This ensures self-consistency and enables us to perform a robust statistical analysis when estimating stellar parameters from a large database of observed spectra.

3.1 A χ^2 estimator

Given a set of observations, estimating the model that best fits the data is a well-known problem in data modelling. The basic approach to solve this problem is generally to choose an estimator and a merit function that describes the agreement between the data and the model, and adjust the parameters of the latter to achieve close agreement. In the rest of this paper, we will be using a maximum likelihood estimator also known as the χ^2 estimator and the Levenberg–Marquardt (LM) algorithm to search through the non-linear dependencies of the model parameters. Levenberg (1944) and Marquardt (1963) have put forth an elegant method to rapidly and efficiently go through the parameter space by adjusting parameters using gradient search and parabolic approximation methods in order to find the ones that minimize the χ^2. However, as with many fitting algorithms, the LM algorithm finds only a local minimum, which is not necessarily the global minimum.

At a high level, this analysis involves finding a suitable model defined by a set of parameters that can describe a given set of observations. In some other analyses of this nature, the parameters we want can be a set of functions directly depending on them. In other analyses, the model depends in a non-trivial way on the selected parameters. With our method LM minimization is used for a subset of the parameters of interest.

3.2 Parameters to fit

Fitting the entire spectral range is computationally expensive and also of limited interest, as spectral lines are largely redundant regarding what they reveal about stellar parameters. Valenti & Fischer (2005) carefully chose nine spectral windows that are sensitive to required stellar parameters ($T_{\rm eff}$, $\log g$, $\log [M/H]$). Brewer et al. (2015) later expanded the list to 20 windows. They added 28 per cent more lines that are $\log g$ sensitive and 51 per cent more that are temperature-sensitive (see Table 1). In this study, we only considered 16 of the 20 proposed windows by Brewer et al. (2015). Two of them were incompatible with PHOENIX. We also removed 5160Å – 5190Å and 5190Å – 5207Å because they contain lines that were not adequately modelled which limited our ability to estimate the parameters – the exact reasons for this are not clear.

The model for $T_{\rm eff}$, $\log g$, $\log [M/H]$ (called global parameters) depends on underlying complex physics models that produce the synthetic spectra. The model for rotation velocity, radial velocity, macro-turbulence, and continuum coefficients (called local parameters) can be expressed as a mathematical operation between the synthetic spectra and a set of functions. As synthesizing a PHOENIX spectrum at every modelling step of the LM algorithm would be too time-consuming, we pre-compute a grid of synthetic spectra and use the LM algorithm to estimate only the local parameters for each observed spectrum. This procedure is carried out on a pre-computed grid of synthetic spectra varying from 5000 to 6000 K, 4.0–5.0 dex and –0.5 to 0.5 dex with steps of 25 K 0.05 dex and 0.05 dex in $T_{\rm eff}$, $\log g$, and $\log [M/H]$, respectively. At every step in $T_{\rm eff}$, $\log g$, $\log [M/H]$, we will map the global parameters space with the resulting χ^2 from the LM fitting of the local parameters for the given spectra. The χ^2 map will then be used to estimate the global parameters, by finding the set of $T_{\rm eff}$, $\log g$, $\log [M/H]$ values that minimizes the χ^2.

Local parameters are directly estimated with the LM algorithm using the corresponding model for each of the fitted parameters. Given that we are fitting different windows in wavelength, each model is computed window by window but fitted simultaneously to the observed spectrum.

Macro-turbulence is an additional spectral broadening that is used to compensate for a macroscopic velocity field ($v_{\rm mac}$) that the 1D stellar model atmospheres fail to capture. It is common to use a radial tangential profile (Gray 1975) to model the macro-turbulence. However, the Takeda & UeNo (2017) study of the non-thermal velocity dispersion along the line of sight with high-resolution solar spectra brings this into question. They analysed spectral lines at different points of the solar disc and found that the non-thermal velocity dispersion followed a nearly normal distribution and concluded that radial tangential profile is not an adequate model, at least for solar-type stars. Based on these findings, we used a Gaussian distribution profile to model the macro-turbulence. Brewer et al. (2016) provided an empirical formula for the macro-turbulence based on observations, it describes the evolution of the macro-turbulence with the $T_{\rm eff}$ and $\log g$. We adjusted their formula so that the solar macro-turbulence is 3.00 km.s^{-1}(FWHM) based on our line calibration done with the Solar spectrum (see Section 4.2.1). The effect of the macro-turbulence can be modelled as a convolution between the synthetic spectrum and a Gaussian macro-turbulent velocity profile.

The $v \sin i$ is the stellar rotational velocity projected along the line of sight. The impact of the rotational velocity of a star on its spectrum can be modelled as an induced macroscopic spectral broadening by the rotational profile. This is modelled by applying a convolution between the given spectrum and the rotation profile (Gray 2005).

The radial velocity of a star relative to the Solar system barycenter induces a shift in wavelength in the spectrum. Estimating the radial velocity shift ($v_{\rm rad}$) is essential to identify the lines and have a good overall agreement between the observed and the fitted synthetic spectra. One should keep in mind that Sun-like stars are composed of convective cells, or granules, where hot gas is rising, and cooler gas is sinking in the intragranular lanes. Therefore, the stellar surface is composed of local blueshifts and redshifts. Since the rising

Table 1. Considered wavelength intervals in Ångström for the Sun, ξ Boo A, and ϵ Eri. We also give the reduced χ^2_L (in the lines), the total reduced χ^2, the number of points in the lines (n_L), and the total number of points (n) (see Section 4.4.3). This gives an idea of the information contained per window.

	Sun						ξ Boo A						ϵ Eri					
λ_{beg}-λ_{end} (Å)	χ^2_L	χ^2	χ^2_L/χ^2	n_L	n	n_L/n	χ^2_L	χ^2	χ^2_L/χ^2	n_L	n	n_L/n	χ^2_L	χ^2	χ^2_L/χ^2	n_L	n	n_L/n
5231.75-5261.94	75.54	38.20	1.98	216	650	0.33	181.28	93.57	1.94	266	647	0.41	1019	657	1.55	366	649	0.56
6004.27-6012.56	40.21	10.72	3.75	33	214	0.15	99.63	26.91	3.70	39	213	0.18	757	251	3.01	44	212	0.21
6016.17-6028.71	22.45	5.31	4.23	31	296	0.10	38.41	8.55	4.49	34	297	0.11	651	140	4.65	46	296	0.16
6031.31-6048.90	11.56	2.98	3.88	4	479	0.01	5.97	3.24	1.84	5	479	0.01	112	32	3.52	14	479	0.03
6051.10-6070.04	14.68	4.52	3.25	28	478	0.06	58.19	8.81	6.61	33	491	0.07	258	75	3.45	52	481	0.11
6099.83-6119.00	158.56	26.19	6.06	62	514	0.12	455.60	71.53	6.37	67	514	0.13	2581	473	5.45	77	514	0.15
6120.69-6139.99	72.76	24.58	2.96	95	492	0.19	168.42	53.76	3.13	114	494	0.23	875	376	2.33	153	493	0.31
6142.89-6158.03	69.42	18.18	3.82	56	429	0.13	60.08	17.59	3.42	58	430	0.13	1152	255	4.51	63	429	0.15
6160.97-6179.60	93.57	28.35	3.30	120	545	0.22	197.66	63.89	3.09	152	545	0.28	1348	523	2.58	190	544	0.35
6310.87-6319.37	78.95	36.22	2.18	54	180	0.30	177.12	95.88	1.85	67	181	0.37	1065	492	2.17	66	180	0.37
6579.52-6599.48	41.37	17.42	2.37	50	459	0.11	297.18	51.09	5.82	56	487	0.11	1953	394	4.96	57	463	0.12
6689.26-6701.42	8.02	6.72	1.19	15	295	0.05	19.25	8.06	2.39	16	295	0.05	220	96	2.29	23	296	0.08
6702.86-6710.07	8.90	5.12	1.74	11	129	0.09	24.75	9.04	2.74	13	129	0.10	408	95	4.31	14	128	0.11
6712.00-6718.90	6.88	4.80	1.43	32	186	0.17	30.56	12.68	2.41	34	186	0.18	395	144	2.74	39	185	0.21
7439.67-7469.90	45.21	15.84	2.85	45	539	0.08	106.47	31.57	3.37	47	539	0.09	493	214	2.31	64	537	0.12
7769.00-7798.28	54.13	9.60	5.64	46	571	0.08	119.36	35.74	3.34	48	571	0.08	988	135	7.33	43	571	0.08
All windows	68.99	17.53	3.94	898	6456	0.14	171.14	40.93	4.18	1049	6498	0.16	1,063.56	298.13	3.57	1311	6457	0.20

hot gas is brighter than the cooler sinking gas, a net blueshift is observed.

All three of the local parameters mentioned so far ($v \sin i$, v_{rad}, and v_{mac}) are assumed not to depend on wavelength.

Synthetic spectra from PHOENIX are divided by a modelled continuum, thus yielding a close to perfect normalization. However, observed spectra are generally normalized by the apparent stellar continuum. The latter is an automated process and the continuum normalization is only an approximation. These different normalizations result in mismatched continuum levels between observed and synthetic spectra. We, therefore, applied an additional normalization correction during the synthetic spectrum fitting procedure to account for these differences. The extra continuum correction can be modelled as a wavelength-dependent function added to the synthetic spectra. Since the wavelength range of our considered spectral windows is never wider than few nanometers, the correction can be approximated by a linear function with two coefficients. As for previous parameters, the model is computed window by window but this time with unique continuum coefficients for each window. This gives us a total of 32 continuum correction coefficients (2 per window) to fit.

Continuum adjustment can go astray if not treated with care and can result in poorly fitted data. For instance, Fig. 3 shows the effect of a badly fitted spectrum. The LM algorithm tried to compensate for inadequate line modelling while trying to minimize the χ^2, which, in turn, leads to a misplaced continuum. The LM algorithm returned a lower χ^2 than suggested by the poor fit to the profiles and therefore created unwanted artificial local minima in the χ^2 map. We can make the LM algorithm more robust to these kinds of issues by fitting the continuum more carefully. To do that, we applied a mask to the observed and the synthetic spectra in order to only consider sections with continuum while computing the derivatives of the correction function required during the fitting process. This ensured that the LM algorithm ignored any differences in the line profiles only while fitting the continuum correction function and the result can be seen in Fig. 3, where the continuum is well placed but with a worse χ^2 that accurately reflects the poor fit to the line profile.

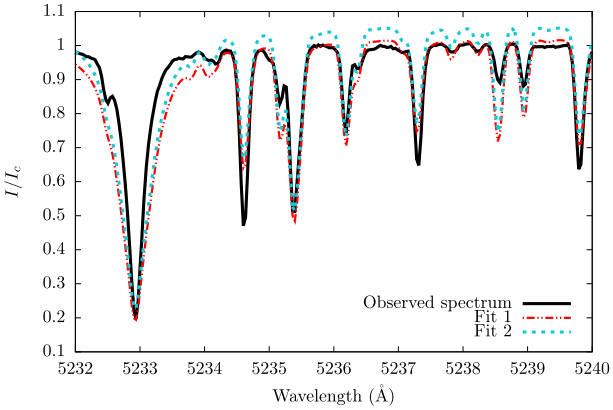

Figure 3. Continuum placement with and without the modified LM code. Fitted synthetic spectra to an observed one (black). Fit 1 (red) corresponds to the modified LM code and Fit 2 (blue) corresponds to the unmodified LM code.

4 FITTING OBSERVED SPECTRA

4.1 Stellar sample

We use observed spectra from the spectropolarimetric observations from PolarBase (Petit et al. 2014). PolarBase is a database that contains all public stellar data collected with ESPaDOnS at the Canada–France–Hawaii–Telescope (CFHT) and its twin, NARVAL, at Télescope Bernard Lyot (TBL), both of which are high-resolution spectropolarimeters (Donati 2003). We used intensity spectra normalized to the apparent continuum processed with Libre–ESpRIT data reduction software (Donati et al. 1997). During the fitting procedure, we correct for any discrepancies due to normalization between observed and synthetic spectra.

Instrumental broadening plays a major role when estimating the stellar broadening, it is then essential to characterize the instrumental profile broadening. The spectral resolution of ESPaDOnS and NARVAL is 68000, the instrumental broadening correspond to a

Gaussian profile with a full width at half-maximum of 4.4 km.s^{-1}. Thus, the instrumental profile is simulated with a Gaussian function with the associated broadening.

In the present paper, we analyse high *S/N* (>100) and high-resolution ESPaDOnS/NARVAL spectra of 17 main sequence dwarfs with spectral types G and K, including the Sun, 18 Sco, HD 4915, and ξ Boo A (see Table 2). The characteristics of the stars in our sample, range from 5000 K to 6000 K in $T_{\rm eff}$, 4.0–5.0 in log g and –0.5 to 0.5 in log [M/H]. They are well-characterized stars in common with Brewer et al. (2016) and ESPaDOnS/NARVAL database.

4.2 Spectral line-list calibration on standard stars

We updated the old PHOENIX atomic line data with the latest line data from the Vienna Atomic Line Database, VALD3 (Piskunov et al. 1995; Kupka et al. 1999; Kupka, Dubernet & VAMDC Collaboration 2011) in early 2017. The database predominantly consists of line data from Kurucz & Bell (1995), but VALD is regularly updated with critically evaluated data sets. We extracted all lines between 5 000 and 8 000Å to be absolutely sure that we did not miss any weak lines. For every line, we used the PHOENIX internal approximation (Schweitzer, Hauschildt & Allard 1996) for Stark, radiative, and van der Waals damping parameters, unless any values were manually changed during the line calibration procedure. The molecular line-list contains lines complied from various sources described in Allard, Homeier & Freytag (2012).

Fig. 4 shows the differences between the old and VALD3 updated line-lists compared to a solar spectrum. It is straightforward to notice that the synthetic spectrum with updated lines fits the solar data better than the synthetic spectrum using the old line-list. In fact, some new lines have been added in the updated line-list and the accuracy in the modelled line strengths has greatly improved. Some lines are still missing even in the updated line-list. We, therefore used a mask to remove them from the fitting process. Despite the clear improvement over the old line-list, the agreement between the observed and the synthetic solar spectrum is still not sufficient to be able to estimate stellar parameters with the precision that we require.

4.2.1 Calibration on the Sun

Accurately modelling every single line is a task that even PHOENIX cannot perform. The underlying physics of stellar atmospheres involves complex process that cannot yet be fully captured within 1D RHD models such as PHOENIX, which, in turn, introduces some errors in synthetic spectra. While some of these errors are due to the fact that the line-list is not as complete nor as accurate as it should be, most of them are due to our inability to correctly model the stellar atmosphere. Both sources of errors can be empirically corrected by updating the new line-list by adjusting the logarithm of oscillator strength (log gf), the van der Waals damping parameter (σ_W) on well-known standards such as the Sun and similar stars.

Our analysis differs from approaches that rely on lines ratios or equivalent width measurements to circumvent these issues. Our method fits the observed spectrum directly, rather than trying to match equivalent widths and allows us to go further and determine $T_{\rm eff}$ and log g from the spectrum itself, making use of the full information contained in high-resolution spectra. The overall improvement of the Solar spectrum fit produced by the VALD3 updated line-list (see Fig. 4) validate this approach.

In our limited spectral range (e.g. Valenti & Fischer 2005; Brewer et al. 2015, 2016), hundreds of lines are inaccurately modelled. In order to efficiently determine an optimal solution to this problem, we have interfaced PHEONIX with a maximum likelihood estimator using the Levenberg–Marquardt algorithm to correct for log gf. At each iteration of the LM algorithm, a new PHOENIX synthetic spectrum was computed, 10 iterations were sufficient to ensure the proper convergence of the LM code.

The corrections we made to the solar model are not unique solutions and so it is essential to calibrate using stars across the entire range of temperatures in our grid in order to reach the optimal corrections.

For the first calibration, we used the following atmospheric parameters for the Sun: $T_{\rm eff} = 5775$ K log $g = 4.44$, log [M/H] = 0.0, $v \sin i = 1.63$ km.s^{-1}(Brewer et al. 2016) and the macro-turbulence was left as a free parameter filling in for any remaining and unaccounted broadening in the system. We found that the macro-turbulence that best fit the data after the calibration on all windows is 3.00 km.s^{-1}(FWHM). For the micro-turbulent broadening, we used the previously mentioned calibration done by Allard et al. (2011) (see Fig. 2), calibrated on 2D RHD simulations. We successfully refined the oscillator strength for over 300 lines (see Fig. A1) using the observed solar spectrum (see Figs A4, A5 for detailed statistics and Figs A6–A14 to see identified lines).

4.2.2 Calibration on ϵ Eri & ξ Boo A

We proceeded with further calibration using ξ Boo A and ϵ Eri which have the following published atmospheric parameters: $T_{\rm eff} =$ 5465 K log $g = 4.54$, log [M/H] $= -0.16$, $v \sin i = 4.4$ km.s^{-1}and $T_{\rm eff} = 5066K$, log $g = 4.57$, log [M/H] $= -0.06$, $v \sin i = 2.4$ km.s^{-1}(Brewer et al. 2016). We calibrated the oscillator strength as well as the van der Waals damping parameter.

Fig. 5 shows the fitted synthetic spectra for the Sun, ξ boo A, and ϵ Eridani. Line profiles are not only accurately modelled but also their evolution as the temperature decreases (spectra of ξ Boo A and ϵ Eridani). We call this procedure 'anchoring the models on standards' (see also Figs A1–A3).

After anchoring our models on these three standards, we can estimate stellar parameters for the stars in our sample.

4.3 Fitting parameters

Stellar parameter estimation is done by evenly mapping the parameter space in terms of χ^2 while fitting $v \sin i$, $v_{\rm rad}$, $v_{\rm mac}$, and the continuum corrections parameters at each point using a maximum likelihood estimator.

When close enough to the minimum, we use a parabolic approximation to fit the points near the χ^2 minimum to find both the accurate location of this minimum and the corresponding error bars. In 3D ($T_{\rm eff}$, log g, and log [M/H] space), this expansion can be written as:

$$\chi^2 = aT^2 + dG^2 + fM^2 + bTG + cTM + eGM + gT + hG + iM + j, \quad (1)$$

where $\{a, b, .., j\}$ are 10 coefficients of the parabolic model to be fitted, $T = T_{\rm eff}$, $G =$ log g, and $M =$ log [M/H]. The χ^2 is at the minimum when:

$$T = (ED - FB)/(AB - DC), \quad (2)$$

Table 2. Estimated $T_{\rm eff}$, $\log g$, $\log [M/H]$, and their final formal uncertainties associated with the same parameters (B) from Brewer et al. (2016). They have an estimated $\Delta T_{\rm eff} = 25$ K, $\Delta \log g = 0.028$ dex, and $\Delta \log [M/H] = 0.01$ dex for every stars. We also added the surface gravity estimated from seismic data (A) from Chaplin et al. (2014); Heiter et al. (2015); Yıldız, Çelik Orhan & Kayhan (2016), if available. $S/N_{\rm eq}$ is the equivalent *S/N* of the fit (*S/N* divided by the $\sqrt{\chi^2_{\rm L}}$).

#Name	$T_{\rm eff}$ (K)	$\log g$ (dex)	$\log [M/H]$ (dex)	vsin i (km.s^{-1})	$T^B_{\rm eff}$ (K)	$\log g^B$(dex)	$\log [M/H]^B$ (dex)	vsin i^B (km.s^{-1})	$\log g^A$ (dex)	S/N	S/N $_{\rm eq}$
Sun	5761 ± 4	4.45 ± 0.008	0.02 ± 0.004	1.60 ± 0.01	5770 ± 25	4.44 ± 0.027	0.00 ± 0.01	1.6 ± 0.5		600	134.16
ξ Boo A	5505 ± 6	4.61 ± 0.006	-0.13 ± 0.005	5.40 ± 0.03	5465 ± 25	4.54 ± 0.027	-0.16 ± 0.01	4.4 ± 0.5		800	79.60
ϵ Eri	5077 ± 6	4.59 ± 0.009	-0.06 ± 0.005	2.48 ± 0.03	5065 ± 25	4.57 ± 0.027	-0.06 ± 0.01	2.2 ± 0.5		1200	76.20
18 Sco	5790 ± 9	4.50 ± 0.017	0.06 ± 0.007	1.92 ± 0.01	5785 ± 25	4.41 ± 0.027	0.04 ± 0.01	1.5 ± 0.5	4.44	1300	115.36
HD 154345	5491 ± 8	4.53 ± 0.027	-0.13 ± 0.013	1.58 ± 0.01	5455 ± 25	4.52 ± 0.027	-0.14 ± 0.01	1.2 ± 0.5		650	91.02
HD 10476	5187 ± 18	4.43 ± 0.021	-0.05 ± 0.012	1.50 ± 0.01	5190 ± 25	4.51 ± 0.027	-0.03 ± 0.01	0.1 ± 0.5		700	62.36
HD 10780	5324 ± 7	4.54 ± 0.010	0.02 ± 0.005	<1.00 ± 0.01	5344 ± 25	4.54 ± 0.027	0.01 ± 0.01	0.8 ± 0.5		1100	77.98
τ Ceti	5429 ± 10	4.49 ± 0.017	-0.41 ± 0.013	<1.00 ± 0.01	5333 ± 25	4.60 ± 0.027	-0.44 ± 0.01	0.1 ± 0.5	4.58	600	88.47
HD 190360	5584 ± 10	4.28 ± 0.019	0.20 ± 0.008	3.00 ± 0.02	5549 ± 25	4.29 ± 0.027	0.19 ± 0.01	2.1 ± 0.5		630	53.63
σ Dra	5246 ± 10	4.51 ± 0.018	-0.25 ± 0.009	1.28 ± 0.01	5242 ± 25	4.56 ± 0.027	-0.21 ± 0.01	0.5 ± 0.5		100	57.74
HD 222582	5800 ± 12	4.39 ± 0.008	0.02 ± 0.007	<1.00 ± 0.01	5789 ± 25	4.38 ± 0.027	0.01 ± 0.01	0.5 ± 0.5		160	80.00
HD 178911 B	5584 ± 12	4.41 ± 0.014	0.21 ± 0.010	3.31 ± 0.01	5564 ± 25	4.40 ± 0.027	0.20 ± 0.01	2.2 ± 0.5		300	52.22
HD 46375	5275 ± 8	4.40 ± 0.011	0.25 ± 0.006	2.50 ± 0.02	5243 ± 25	4.43 ± 0.027	0.23 ± 0.01	1.3 ± 0.5		555	54.16
HD 97658	5162 ± 6	4.51 ± 0.010	-0.27 ± 0.004	1.50 ± 0.01	5120 ± 25	4.57 ± 0.027	-0.25 ± 0.01	0.1 ± 0.5		811	85.97
HD 9540	5447 ± 4	4.61 ± 0.016	-0.06 ± 0.013	<1.00 ± 0.01	5417 ± 25	4.54 ± 0.027	-0.07 ± 0.01	0.8 ± 0.5		723	68.62
HD 24496	5526 ± 10	4.52 ± 0.014	-0.02 ± 0.007	<1.00 ± 0.01	5531 ± 25	4.50 ± 0.027	-0.05 ± 0.01	0.1 ± 0.5		319	75.19
HD 173701	5332 ± 18	4.39 ± 0.019	0.27 ± 0.009	2.60 ± 0.02	5342 ± 25	4.36 ± 0.027	0.29 ± 0.01	2.2 ± 0.5	4.48	500	46.03

$$G = (IA - BH)/(AD + BG), \tag{3}$$

$$M = (KA - LD)/(-DB - AJ), \tag{4}$$

where:

$$A = 2ae - cb, \qquad B = 2bf - ce, \qquad C = 4af - c^2 \tag{5}$$

$$D = be - 2dc, \qquad E = 2fg - ci, \qquad F = ge - hc \tag{6}$$

$$G = b^2 - 4da, \qquad H = gb - 2ah, \qquad I = hc - ib \tag{7}$$

$$J = e^2 - 4df, \qquad K = he - 2di, \qquad L = ge - ib. \tag{8}$$

Finding the optimal stellar parameters is then a matter of estimating the paraboloid coefficients close enough to the minimum of the χ^2 map.

The χ^2 function is constructed in such a way that if the errors on the data set are normally distributed and the model used is perfect, then the minimum χ^2 should on average be equal to the number of points N – 35 in the data set (number of points minus the degrees of freedom). The constraint is almost never verified considering that we can have various sources of errors that are either not quantified and/or do not follow the normal distribution, we call them systematic errors. We discuss how to deal with this problem in the next subsection. Now that we can estimate the minimum χ^2 and therefore the stellar parameters, the uncertainties on these parameters must be estimated. We describe this procedure in the following section.

4.4 Error analysis

We describe the derivation of error bars and demonstrate their reliability.

4.4.1 *Sytematic errors versus signal to noise (S/N)*

When modelling data, we can separate errors in to two categories: photon noise and any other errors (systematic errors), both of which increase the uncertainties in parameter estimation. It is necessary to assess the impact of both of these sources of errors and characterize their relative weights. We selected spectra of the Sun, ξ Boo A, and ϵ Eri with respective *S/N* of 600, 1400, 1200 and we gradually increased the noise.

Fig. 6 shows the formal uncertainties plotted against increasing *S/N*. At low *S/N*, the formal error bars decrease as the noise decreases, which is expected. The formal uncertainties are sensitive to photon noise when the latter is dominant (e.g. at low *S/N*). The formal error scatter is relatively flat for $S/N > 150$. This indicates the transition where the systematic error dominates the whole estimation procedure. In Table 2, $S/N_{\rm eq}$ gives the equivalent signal to noise at which we are fitting the data.

4.4.2 *Effect of vsin i on the uncertainties*

The rotation of the star impacts the stellar parameter estimation. At high spectral resolution, and with rapidly rotating stars, the line broadening can be dominated by the projected rotational broadening. It directly impacts the smaller lines by blending them with nearby deeper lines. It also blurs the detailed shape of the spectral line; information is lost even in the absence of blending. To assess the impact of rotational broadening on the parameter estimation, we artificially broadened a synthetic spectrum and, for various vsin i, presented the recovered stellar parameters with the associated uncertainties through our estimation tool.

Fig. 7 shows the formal uncertainties against the vsin i. vsin i becomes a limiting factor when it has about the same value as the intrinsic line broadening, the transition occurs at about 10 km.s^{-1}, which is what one would expect. The formal error bars increase rapidly as the vsin i increases and dominate the systematics. This shows that blending due to rotational broadening is a limiting factor on the precision that we can achieve.

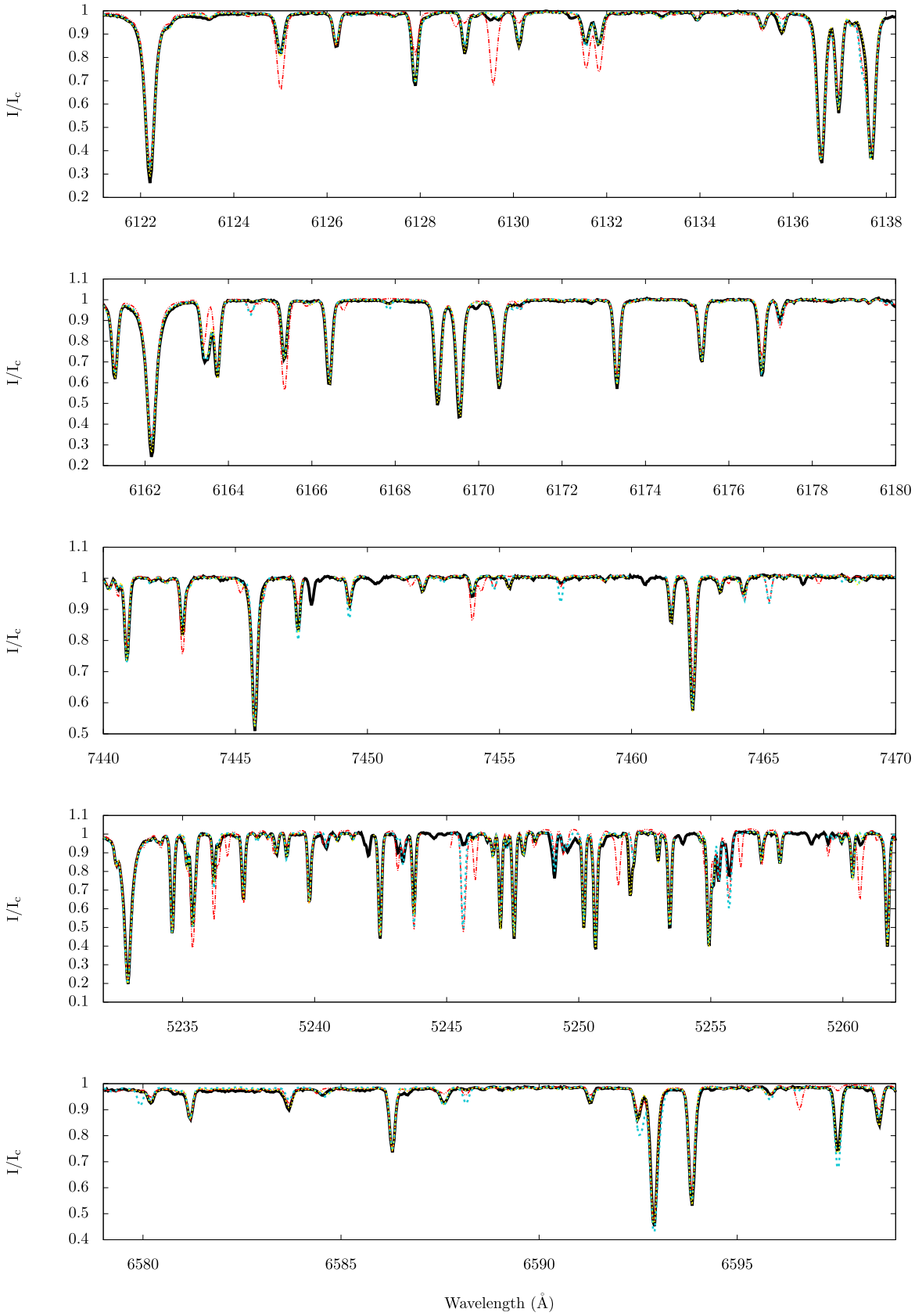

Figure 4. Synthetic spectrum with original (red), updated VALD (blue), and corrected VALD (yellow) line-list parameters compared to an observed spectrum of the Sun (black).

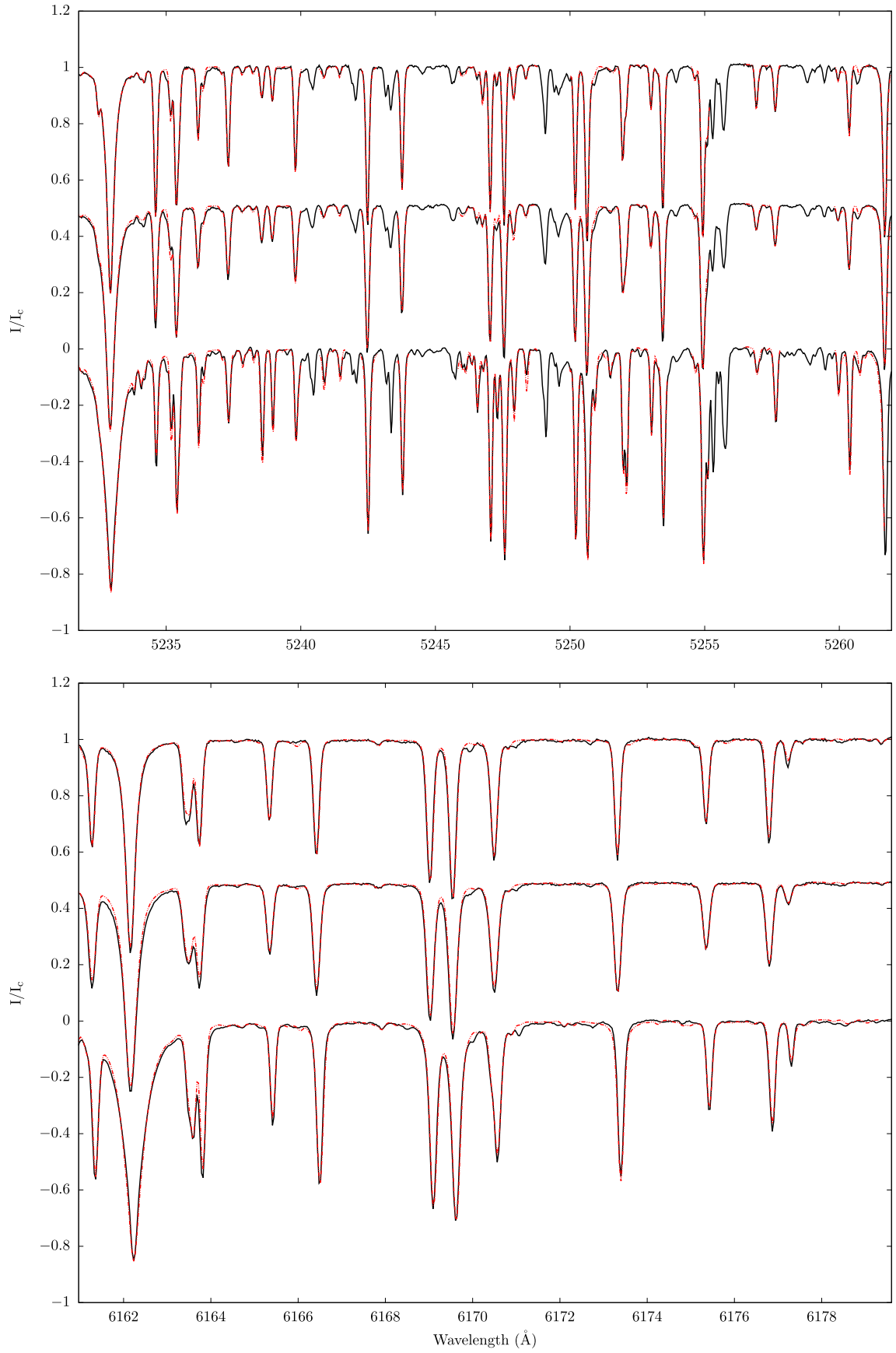

Figure 5. Synthetic (red) against observed (black) spectrum post calibrations. From top to bottom, we have the Sun, ξ Boo A, and ϵ Eri. The ξ Boo A and ϵ Eri spectra are vertically shifted.

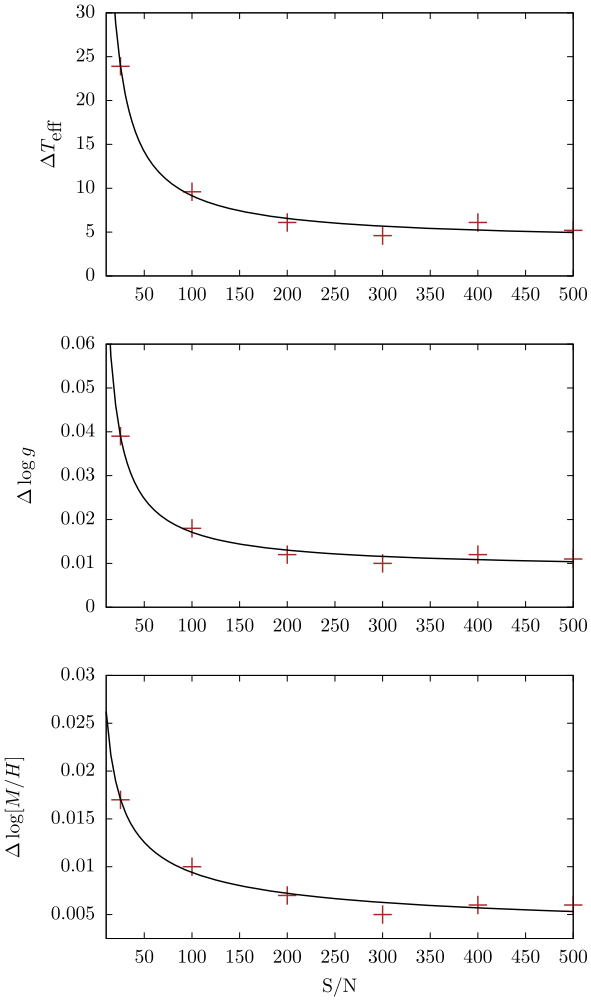

Figure 6. Error bars as a function of the *S*/*N* for artificially noised data with the associated fitted function using the three sets of data. $T_{\rm eff}$ is the top figure, $\log g$ is the middle figure, and $\log [M/H]$ is the bottom figure. We have spectra of the Sun (red) with *S*/*N* of 600.

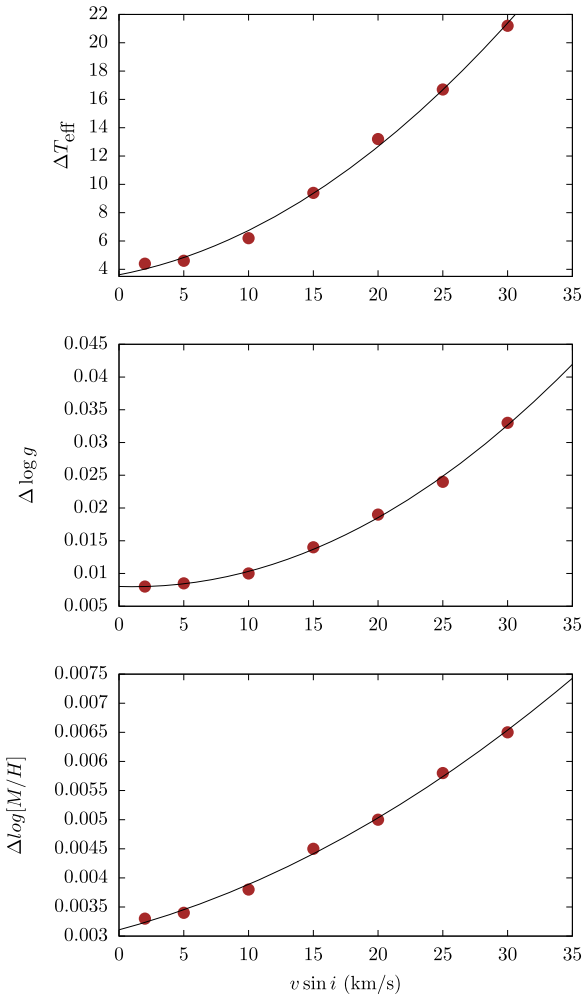

Figure 7. Formal error bars as a function of the $v \sin i$ computed with a synthetic solar spectrum.

4.4.3 *Formal error analysis*

In the previous section, we described how we estimated the parameters using a χ^2 map of the parameter space. The main advantage of producing these maps is that it is straightforward to estimate error bars. Following Press et al. (1992), the 1σ interval is obtained when the χ^2 increases by 1 relative to the minimum assuming the model provides a proper description of the data down to the noise level. Therefore, the confidence interval for each parameter is naturally the projection of the 3D confidence interval on the 1D parameter space. The simplest way to evaluate this projection (and thus the formal error bars) is to compute the curvature radii at the χ^2 minimum. Using equation (1), the expression of the error bars simply becomes:

$$\Delta T = (2a + 2b\beta_{\rm T} + 2c\alpha_{\rm T} + 2d\beta_{\rm T}^2 + 2e\alpha_{\rm T}\beta_{\rm T} + 2f\alpha_{\rm T}^2)^{-0.5}, \quad (9)$$

$$\Delta G = (2d + 2e\beta_{\rm G} + 2b\alpha_{\rm G} + 2f\beta_{\rm G}^2 + 2c\alpha_{\rm G}\beta_{\rm G} + 2a\alpha_{\rm G}^2)^{-0.5}, \quad (10)$$

$$\Delta M = (2f + 2c\beta_{\rm M} + 2e\alpha_{\rm M} + 2a\beta_{\rm M}^2 + 2b\alpha_{\rm M}\beta_{\rm M} + 2d\alpha_{\rm M}^2)^{-0.5}, \quad (11)$$

where:

$$\alpha_{\rm T} = -D/J \quad \beta_{\rm T} = -(b + e\alpha_{\rm T})/(2d) \quad (12)$$

$$\alpha_{\rm G} = -B/C \quad \beta_{\rm G} = -(e + c\alpha_{\rm G})/(2f) \quad (13)$$

$$\alpha_{\rm M} = A/G \quad \beta_{\rm M} = -(c + b\alpha_{\rm M})/(2a). \quad (14)$$

The resulting uncertainties on stellar parameters are too small to have any physical meaning, for example 0.2 K. Which is not surprising considering the fact this error analysis method only holds if the input uncertainties on the data are normally distributed and independent. While this may be reasonable if only considering photon noise, it does not account for the systematics (i.e. everything that cannot be accurately modelled). Quantifying the uncertainties due to systematics (i.e. the models are not perfect) might help us to better constrain the error bars on the stellar parameters.

A natural way of quantifying uncertainties between the synthetic and observed spectrum is the reduced χ^2, which estimates the difference between the model and the data set. The continuum accounts for at least 70 per cent of any spectrum in the considered wavelength windows. Since the continuum can be fitted relatively easily and it accounts for about 70 per cent of the number of points,

it can easily dominate the reduced χ^2 and not represent the actual goodness-of-fit of the lines between the synthetic and observed spectrum. We therefore, computed the reduced χ^2 in the lines by only taking any lines deeper than 5 per cent of the continuum; as expected this led to a considerably larger reduced χ^2 (by a factor 3) than when including the continuum. Instead of using the initial uncertainty as it is, we rescaled the latter using the reduced $\sqrt{\chi^2_L}$ in the lines, thus ensuring the normal distribution of the initial uncertainties so that the reduced χ^2 at the minimum is 1 on average. Table 2 summarizes our findings.

4.4.4 *Statistical error analysis*

In order to determine how consistent our final formal error bars on the stellar parameters are, we independently estimated the error bars on the stellar parameters using an empirical statistical standard variation estimator.

The systematics are not random, and are inherently tied to the spectral windows and the synthetic spectra that we use. Re-sampling our observed spectrum by randomly removing one or more spectral windows should characterize the impact of the systematics on the parameter estimation (similar to bootstrapping). However, each spectrum drawn from this randomly re-sampled distribution does not contain the same amount of information (same number of points) because of the difference in window size. In fact the estimated error-bars are over-estimated and should evolve with the number of points used to estimate them. We decided to re-sample the observed spectra randomly 200 times by keeping a fraction (40 per cent 50 per cent, 60 per cent, 70 per cent, and 80 per cent) of the initial number of points. We then estimated the parameters for those 200 spectra for each per cent of data kept and compute the standard deviation of the parameters for each per cent, which we call 'the statistical errors'.

The advantage of re-sampling this way is to be able to quantify both the impact of each window and the impact of imperfect synthetic spectra (systematics) on the stellar parameter estimates. One issue with re-sampling by removing windows is being able to remove enough windows so that we can see the impact of the systematics statistically. The entire procedure followed can be summarized as follows: randomly select the appropriate number of windows of an observed spectrum so that 40 per cent of initial number of point (N) is kept ($\pm$3 per cent) for 200 combinations; subject these 200 sets of spectra to the estimation tools by carefully weighting each χ^2 map accordingly; compute the empirical standard deviation from the 200 stellar parameters estimated for each observed spectrum; repeat the previous steps for per cent50, per cent60, per cent70 and per cent80. Note that this method cannot improve our first estimates of stellar parameters as it does not give any new information on the true stellar parameters.

Fig. 8 shows the results of the statistical errors estimation by randomly re-sampling by only keeping a fraction of the initial number of points of the observed spectrum as well as the associated formal errors. The green line is the fit of the statistical error as a function of the fraction of the kept number of points with the function $f(x) = ax^{-b} + c^2$, where a, b and c are the coefficients to fit. This analysis was conducted on the Sun, ξ Boo A, and ϵ Eri. Extrapolating the decreasing trend of the statistical errors should give reliable statistical error bars for 100 per cent of the initial data points, and the actual statistical uncertainties on the parameters. The fit extrapolation is only here to give an idea of the statistical uncertainties. Comparing formal and statistical errors illustrates the relative agreement of these two methods of error estimations. Indeed, in the worst case scenario, there is only a 30 per cent difference between the two types of estimation. This suggests that the formal errors we computed are reliable and consistent with a pseudo Monte Carlo (statistical) analysis. Results from this statistical error analysis are summarized in Table 2. Furthermore, to assess the accuracy of the returned parameters, Brewer et al. (2015) analysed 20 spectra taken from 4 different asteroids. They recover the solar parameters with an rms scatter of 5 K, 0.006 dex, and 0.003 dex in $T_{\rm eff}$, log g, and log [M/H], respectively, which is consistent with our error bars for the Sun (see Table 2).

One should note that the provided uncertainties are as good as the initial error bars on the three anchor stars. Errors on those parameters would cascade through the estimation procedure for the rest of the sample.

5 ESTIMATED STELLAR PARAMETERS

5.1 Uncertainties on the parameters

In Table 2, we list the stellar parameters found by this study with the associated error bars on each parameters, showing both theoretical and statistical uncertainties and we compare them to published values from Valenti & Fischer (2005); Brewer et al. (2015, 2016). Fig. 9 shows distribution of our sample in the $T_{\rm eff}$ – log g and $T_{\rm eff}$ – log [M/H] planes. Most of them are within the solar metallicity and surface gravity, which is expected since we are only covering main sequence stars.

As discussed in Section 4.4.3, we rescaled the initial photon noise with the reduced χ^2 in the lines, which is how we define the final formal error bars provided in Table 2. The formal uncertainties are 9 K, 0.014 dex, and 0.008 dex on average for $T_{\rm eff}$, log , and metallicity, respectively.

We do not provide uncertainties on vsin i ; they can be directly estimated from the covariance matrix of the best fit but are unreliable. They are unrealistically small, given the fact that vsin i is degenerate with the macro-turbulence and surface gravity, especially at low vsin i . In any case, due to the degeneracies, error-bars on vsin i are inherently problematic.

The final and statistical uncertainties are very similar for the Sun, ξ Boo A, and ϵ Eri as seen in Fig. 8. The statistical uncertainties account for the systematics in the computation of the error bars. Therefore, the similarities between the final and the statistical uncertainties suggest that, even in the worst case scenario, the formal uncertainties rescaled as described in Section 4.4.3 can be used to approximate the actual uncertainties (including the systematics) on the parameters. We give the final uncertainties as only an estimate of the actual uncertainties.

5.2 Comparison to other studies

Comparing the estimated stellar parameters from our analysis to known stellar parameters is an essential but difficult step to validate the method. Indeed, most published stellar parameter analyses are model- and method-dependent and the parameters were not estimated uniformly. Studies for which one method is applied consistently to a large sample, such as Valenti & Fischer (2005); Brewer et al. (2015, 2016); where the stellar parameters have been estimated uniformly, using a similar method, can be used for comparison. It would also be interesting to compare with studies of smaller samples that determine accurate parameters from interferometric measurements, photometry, and stellar models (Boyajian et al. 2013; Ligi et al. 2016).

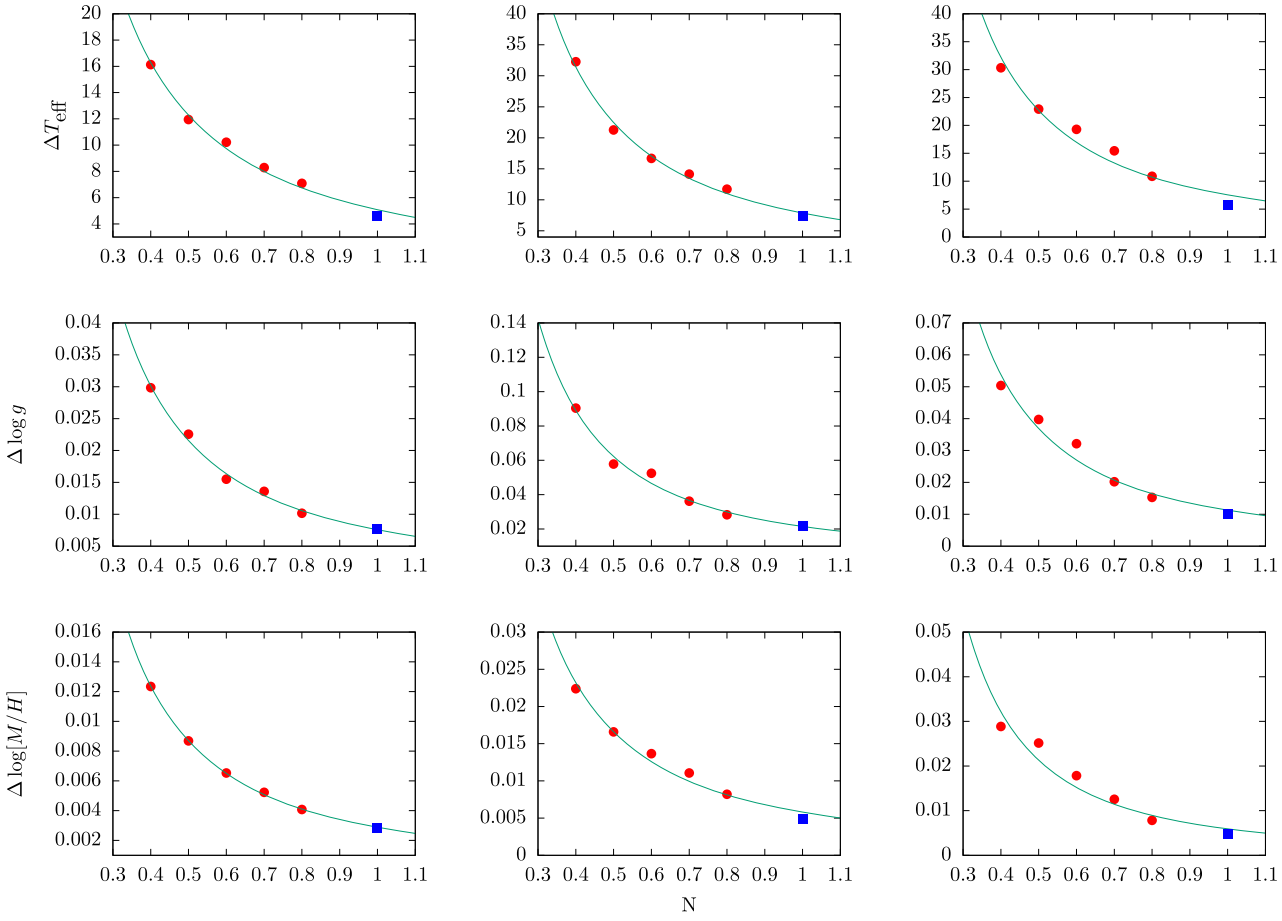

Figure 8. Estimated statistical errors as a function of N (the fraction of the initial number of points used to compute them) in a log/log scale. From left to right we have the Sun, ϵ Eri, ξ Boo A and from top to bottom: $\Delta T_{\rm eff}$, $\Delta \log g$, and $\Delta \log [M/H]$. In red are statistical errors, in green their polynomial fit, and in blue the corresponding formal errors.

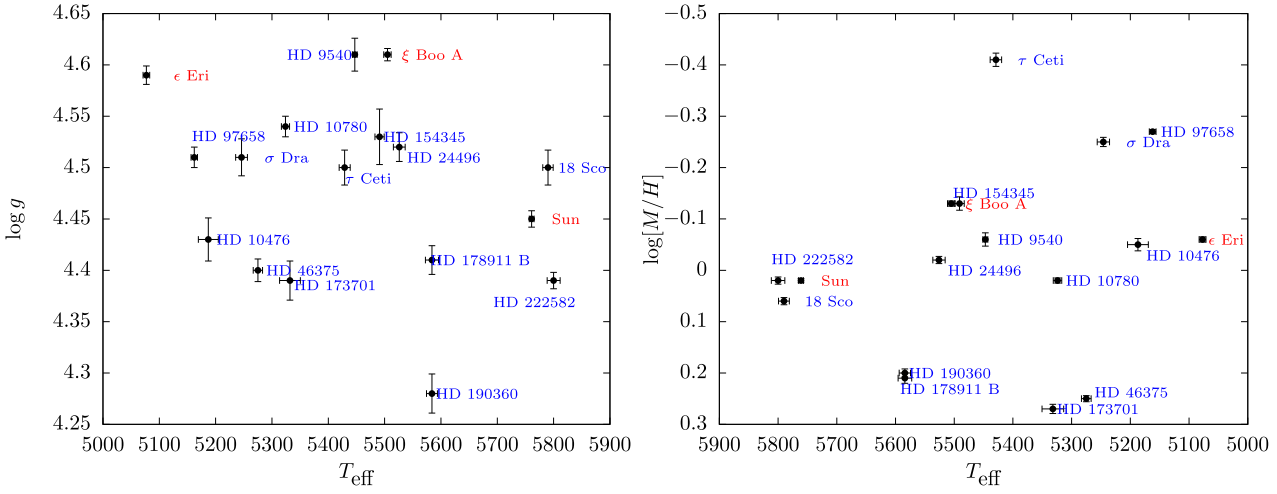

Figure 9. Our star sample plotted with estimated $T_{\rm eff}$ against log [M/H] (right) and log g (left) with associated uncertainties in both directions. We label in red the calibrators that we used.

5.2.1 Brewer et al. (2016) catalog

In Table 2, we list the stellar parameters and error bars from Brewer et al. (2016) (BFVP hereinafter) for the stars studied in this paper. They estimated mean statistical uncertainties of 25 K in $T_{\rm eff}$, 0.028 dex in log g, and 0.01 dex in log [M/H]. These values are compared with ours in Figs 10–12.

There is a relative good agreement between the temperatures obtained from BFVP and this study. The temperatures are within

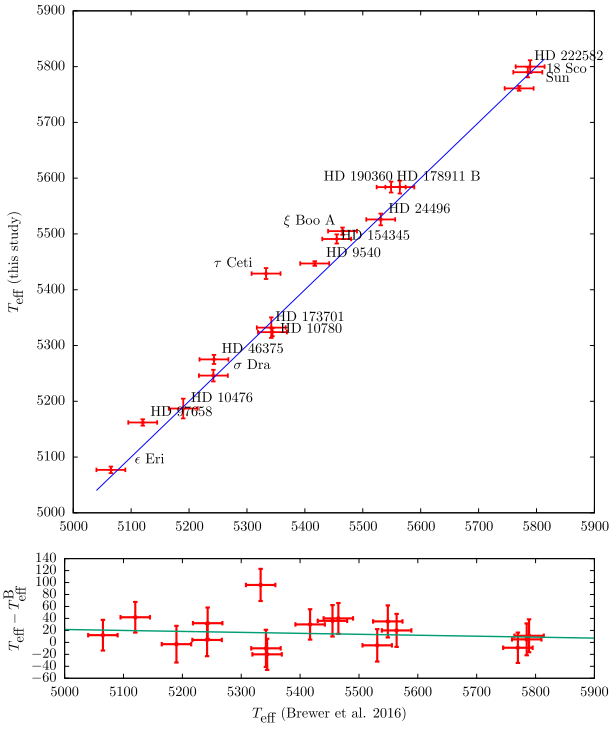

Figure 10. A comparison (top) and difference (bottom) plot of the effective temperature between the parameters from our study and Brewer et al. (2016), the blue line is the $y = x$ line. The green line is the associated linear fit. The standard deviation estimated using sigma clipping on the dispersion is 20 K.

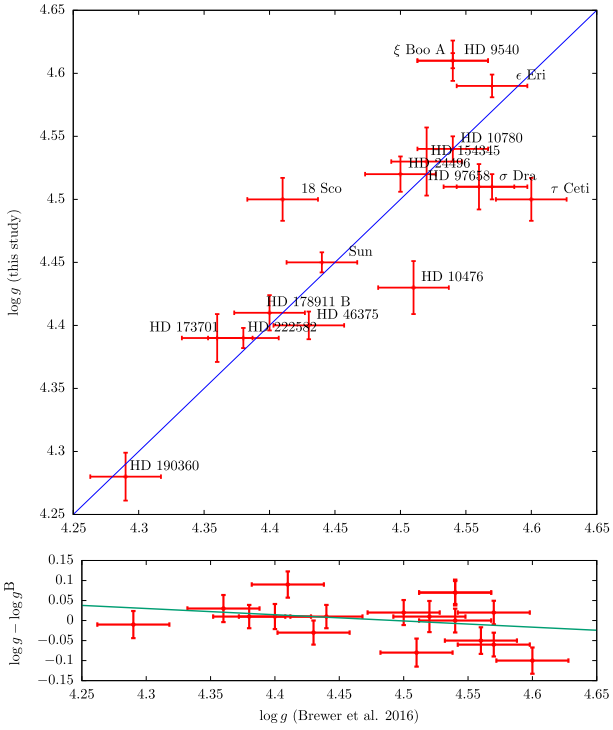

Figure 11. A comparison (top) and difference (bottom) plot of the surface gravity between the parameters from our study and Brewer et al. (2016) the blue line is the $y = x$ line. The green line is the associated linear fit. The standard deviation on the dispersion is 0.05 dex.

the $3\sigma^B$ (except for τ Ceti) range for every star; here, σ^B refers to the errors quoted in BFVP. We find a scatter in temperature of 20 K and an offset of 13 K (see Fig. 10). The offset is predominant for cooler stars (under 5600 K); this suggests that our additional anchoring process on ξ Boo A might be the culprit. But it would be necessary to test this on a larger sample to see if the offset persists. The effective temperature is discrepant for τ Ceti between BFVP and this study. For τ Ceti, the error on $T_{\rm eff}$ is is a direct consequence of the error on $\log g$ since both parameters are correlated (see Fig. 13). However, our temperature estimation is consistent with the literature value and is within 3σ and 1σ variation from spectroscopic and photometric analyses, respectively, Heiter et al. (2015) showed that the mean temperature from various spectroscopic estimations is at 5326K with standard deviation of 45K (12 studies) and the mean temperature from photometric estimations is at 5395K with a standard deviation of 92K (5 studies). The close agreement of the dispersion between the two studies (20 K) with the error bar provided by BFVP (25 K) further supports that the error bars on the estimations of this study, is in fact, smaller or they would add quadratically in the dispersion.

Comparison between the surface gravities (see Fig. 11) shows that there is an overall good agreement between the two studies and a systematic linear trend with the effective temperature (see Fig. 13). However, the dispersion is too large and the sample size is too small to give a definite answer on the trend, a further analysis on a larger sample is needed. Every star falls within the 3σ (Brewer et al. 2016) range. We find a scatter of 0.05 dex and a non-significant offset. The observed discrepancy for τ Ceti might have several origins. This issue may be due to degeneracy between the macro-turbulence, $v \sin i$ and the surface gravity and/or the fact that we removed the window from 516.5 nm to 519.0 nm, which contains $\log g$ sensitive magnesium lines. τ Ceti is known to be a slow rotator (under 2 km.s^{-1}), at this level of rotation, the blending by broadening should be treated with care. But the overall dispersion between the two studies (0.05 dex) agrees with the error bar provided by BFVP (0.028 dex).

Fig. 12 (lower panel) shows a comparison in metallicity between BFVP and our study with an overall good agreement. There is a systematic abundance difference between the stars hotter than 5400 K and those cooler that creates trend with the effective temperature (see Fig. 13). Every star is within the $3\sigma^B$ (Brewer et al. 2016) range and the scatter is 0.022 dex and a non-significant.The close agreement of the dispersion in metallicity, between this study and BFVP, with their error bar (0.01 dex) indicates the consistency of our method, considering that the individual abundances are not fitted, unlike in BFVP.

Given that it is really hard to estimate vsin i with precision, especially for very slow rotators, our estimates are in good agreement with BFVP. The dispersion between the two studies is 0.74 km.s^{-1}, which gives an idea of the uncertainties in the vsin i we should expect.

We notice an overall improved precision by a factor 2.8 in $T_{\rm eff}$, 2.0 in $\log g$, and 1.25 in $\log [M/H]$ compared to BFVP. We were able to achieve this level of precision by carefully treating the line-list and systematics.

Furthermore, 18 Sco, τ Ceti, and ϵ Eri are three of Gaia F–G-K benchmark stars in Heiter et al. (2015). They have estimated $T_{\rm eff}$ and $\log g$ in a systematic way from a compilation of angular diameter measurements and bolometric fluxes and from a homogeneous mass determination based on stellar evolution models. They have found

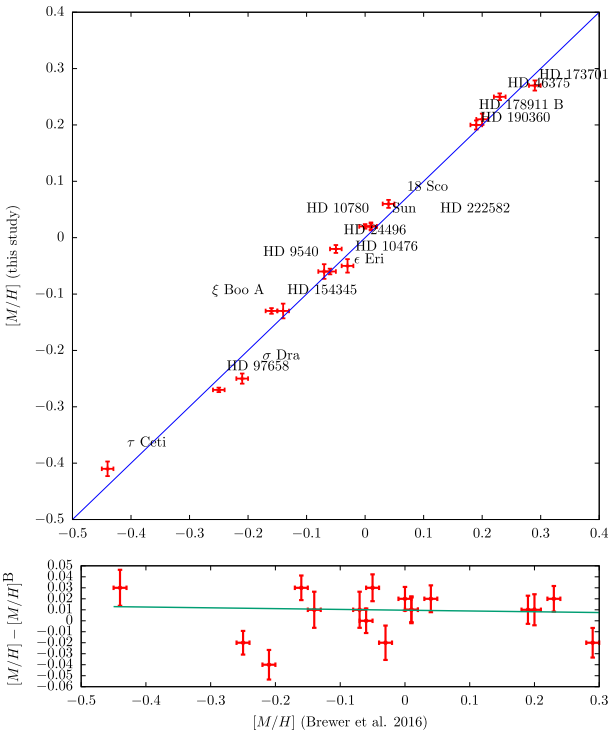

Figure 12. A comparison (top) and difference (bottom) plot of log [*M*/*H*] between the parameters from our study and Brewer et al. (2016) the blue line is the $y = x$ line. The green line is the associated linear fit. The standard deviation on the dispersion is 0.022 dex.

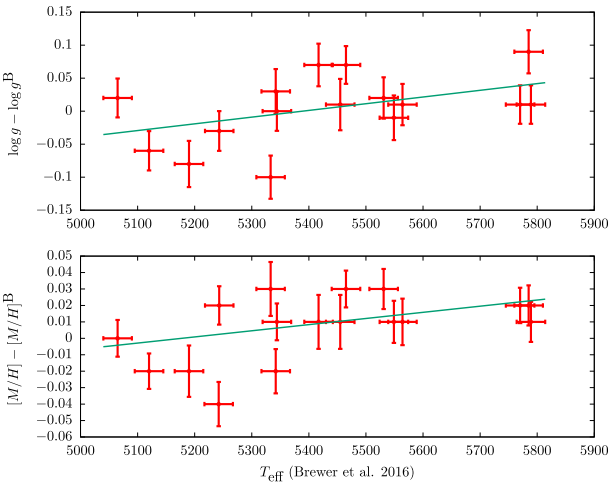

Figure 13. Difference plots between our parameters and those of Brewer et al. (2016) for log *g* (top) and log [*M*/*H*] (bottom). The green line is the $y = x$ line.

$T_{\rm eff} = 5810 \pm 80$ K - $\log g = 4.44 \pm 0.03$ dex, $T_{\rm eff} = 5414 \pm 21$ K - $\log g = 4.49 \pm 0.02$ dex and $T_{\rm eff} = 5076 \pm 30$ K - $\log g = 4.61 \pm 0.03$ dex respectively for 18 Sco, τ Ceti and ϵ Eri. Casagrande et al. (2014) have estimated the effective temperatures derived via the infrared flux method to the interferometric scale for HD 173701. They have found $T_{\rm eff} = 5357 \pm 91$ K. As reported in Table 2, our estimates are highly consistent with their findings, our results are within the 1-σ error bar.

6 CONCLUSION

6.1 Summary

We uniformly analysed 17 spectra of cool stars and successfully derived $T_{\rm eff}$, $\log g$, and $\log [M/H]$ using PHOENIX stellar model atmospheres and spectra from PolarBase. We achieved a mean (χ^2-weighted) precision of $\Delta T_{\rm eff}$=9 K, $\Delta \log g$=0.014 dex, and $\Delta \log [M/H]$=0.008 dex (an improved precision by a factor 2.8 in $T_{\rm eff}$, 2.0 in $\log g$ and 1.25 in $\log [M/H]$ compared to Brewer et al. (2016)). In order to attain this precision, we calibrated over 300 atomic lines using the Sun, ξ Boo A, and ϵ Eri as standards in the spectral ranges specified in Table 1 . We empirically adjusted, the oscillator strength and the van der Waals dampening parameter to reproduce the observed spectra of the Sun, ξ Boo A, and ϵ-Eri at aN *S*/*N* level of 100 (see Figs 5 and 6). We compared the results of this study with Brewer et al. (2016) and confirmed our results were in agreement. This study shows that a systematic calibration of the line-list can be done on a large scale and it improves the precision of stellar parameters estimation.

We provide reliable error bars that have been cross-validated with a pseudo Monte Carlo statistical analysis (see Fig. 8). We applied a random sampling method to spectra of the Sun, ξ Boo A, and ϵ Eri to produce 800 spectra for each star. We subjected the 800 sampled spectra of each star to our estimation procedure and estimated statistical error bars on the parameters. The error bars were within a 30 per cent of the statistical errors at worst. One should note that we do not provide any mathematical proof of the correctness of the uncertainties. Formal errors do not take into account modelling errors, so correcting them empirically becomes a necessity.

Our spectroscopic analysis method is self-consistent, uniform and does not require any prior estimation of the stellar parameters as it estimates the $T_{\rm eff}$, $\log g$ and $\log [M/H]$ simultaneously. This ensures that we avoid any systematic trends depending on priors and achieve a relatively better precision that of Brewer et al. (2016). Our method primarily differs from that of Brewer et al. (2016) in two respect: we use spectra computed using the PHOENIX model atmospheres (as opposed to Kurucz model atmospheres) and we calibrated the line-list on multiple standard stars. But in both cases, the use of a maximum likelihood estimator prevents us from eliminating local minima. The degeneracy between various broadening parameters and the surface gravity results in relatively discrepant gravity estimates for τ Ceti depending on the study.

Recio-Blanco, Bijaoui & de Laverny (2006) proposed an automated procedure for the derivation of stellar atmospheric parameters suited for large sample analysis. The homogeneous and self-consistent nature of our method allows us to achieve a more rapid, precise and uniform spectral classification of large samples stars. This provides key information for planet searches and enables a detailed exploration of many other fields in astrophysics. The stellar parameters are a means of constraining stellar evolution models. The chemical composition of stars can be used to constrain Galactic evolution models.

As discussed in Jofré et al. (2017), the estimated parameters and their uncertainties are as good as the initial error bars on the three anchor stars and highly depend on the method and models. The calibration on the line-list is only accurate for PHOENIX model atmospheres with the same micro-physics.

6.2 Perspective

It is difficult to estimate stellar radii and masses precisely without having well constrained stellar parameters. The standard way to estimate them is to match stellar evolution models with the observed stellar atmospheric parameters, estimated from spectroscopic or photometric analysis (Takeda et al. 2007). Advances in observational asteroseismology also give us a new way of estimating stellar radii and masses (Ulrich 1986; Christensen-Dalsgaard 1993; Chaplin et al. 2008; Stello et al. 2009), but seismic data are not available for most stars. The determination of precise stellar masses and radii obtained by matching observed stellar parameters ($T_{\rm eff}$, $\log g$, and $\log [M/H]$) are subject to errors directly coming from uncertainties on these parameters.

The uncertainties on $T_{\rm eff}$, $\log g$, and $\log [M/H]$ propagate all the way through to the stellar masses and radii estimation. The absence of seismic data increases the uncertainties on the mass and radius up to 50 per cent in the worst case scenario. Spectroscopic estimation of the atmospheric stellar parameters yield on average a $\Delta T_{\rm eff}$=50 K $\Delta \log g$=0.1 dex and $\Delta \log [M/H]$=0.1 dex. For this set of uncertainties the 1σ uncertainties on the mass and radius represent 8 per cent and 12 per cent errors respectively (Basu et al. 2012). Precise estimation with reliable error bars on the atmospheric stellar parameters (such as the ones in this study, $\Delta T_{\rm eff}$=9 K, $\Delta \log g$=0.014 dex, and $\Delta \log [M/H]$=0.008 dex) are key to improve mass and radius estimates.

These promising results encourage us to pursue our main goal which is to model even cooler stars (M dwarfs) to probe the physics of K-M stars, and to even cooler objects to probe the sub-stellar boundary. Previous studies have estimated stellar parameters of M dwarfs (Casagrande et al. 2008; Gaidos et al. 2013; Mann et al. 2015), but never with a systematic and simultaneous estimation of all the stellar parameters using high-resolution synthetic spectra. The improvement we obtained in this study was mainly due to a systematic calibration of the synthetic spectra on standard stars. We will apply the same calibration on stars between 4000 K and 5000 K, and extend the wavelength range to include the optical and the near-infrared range using calibration on both atomic and molecular line-list. And as previously, we will carefully choose standard stars in that range to anchor the line-lists. In order to go in the range of 2500 K and 4000 K the molecular line-list should be particularly treated and calibrated on relatively well known stars with F-G-K companion, as they provide a better estimation of the metallicity. As the anchoring process is only as good as the initial estimates for the anchor stars, it is important to use independent method to calibrate and estimate the stellar parameters of the chosen anchor stars. Instruments such as TESS (Ricker et al. 2014) or GAIA (Lindegren & Perryman 1996) will be essential to complement and improve existing independent methods based on asteroseismology or interferometry and parallaxes.

The objective is to estimate the stellar parameters of M dwarfs using this robust method to attain a similar degree of precision as we have demonstrated here for G-K stars. It is crucial to have accurate line data (see Section 4.2 and Fig. 4) to model stellar spectra. The extension of our study will greatly benefit from ongoing studies on molecular data, both theoretical (McKemmish, Yurchenko & Tennyson 2016) and experimental (Crozet et al. 2014).

ACKNOWLEDGEMENTS

The authors gratefully acknowledge funding by IDEX (Initiative d'excellence) initiative at Université Fédérale Toulouse Midi-Pyrénées (UFTMiP) for making this study possible. The simulations were run on the EOS supercomputer at CALMIP, Toulouse, France. We warmly thank Colin Folsom and Boris Dintrans for their inputs in this work. Finally, the authors would like to thank the reviewer for his thorough review of this study.

REFERENCES

Allard F., Hauschildt P. H., 1995, ApJ, 445, 433
Allard F., Homeier D., Freytag B., 2011, in Johns-Krull C., Browning M. K., West A. A., eds, Astronomical Society of the Pacific Conference Series Vol. 448, 16th Cambridge Workshop on Cool Stars, Stellar Systems, and the Sun, San Francisco, p. 91
Allard F., Homeier D., Freytag B., 2012, Phil. Trans. R. Soc., Lond. Ser. A, 370, 2765
Baraffe I., Homeier D., Allard F., Chabrier G., 2015a, A&A, 577, A42
Baraffe I., Homeier D., Allard F., Chabrier G., 2015b, A&A, 577, A42
Basu S., Verner G. A., Chaplin W. J., Elsworth Y., 2012, ApJ, 746, 76
Böhm-Vitense E., 1958, ZAp, 46, 108
Bonfils X. et al., 2013, A&A, 549, A109
Boyajian T. S. et al., 2012, ApJ, 757, 112
Boyajian T. S. et al., 2013, ApJ, 771, 40
Brewer J. M., Fischer D. A., Basu S., Valenti J. A., Piskunov N., 2015, ApJ, 805, 126
Brewer J. M., Fischer D. A., Valenti J. A., Piskunov N., 2016, ApJS, 225, 32
Bruzual G., Charlot S., 2003, MNRAS, 344, 1000
Casagrande L. et al., 2014, MNRAS, 439, 2060
Casagrande L., Flynn C., Bessell M., 2008, MNRAS, 389, 585
Chaplin W. J. et al., 2014, ApJS, 210, 1
Chaplin W. J., Houdek G., Appourchaux T., Elsworth Y., New R., Toutain T., 2008, A&A, 485, 813
Christensen-Dalsgaard J., 1993, in Weiss W. W., Baglin A., eds, Astronomical Society of the Pacific Conference Series Vol. 40, IAU Colloq. 137: Inside the Stars. San Francisco, CA, p. 483
Crozet P., Dobrev G., Richard C., Ross A. J., 2014, J. Mol. Spectrosc., 303, 46
Demory B.-O. et al., 2009, A&A, 505, 205
Donati J.-F., 2003, in Trujillo-Bueno J., Sanchez Almeida J., eds, Astronomical Society of the Pacific Conference Series Vol. 307, Solar Polarization. San Francisco, CA, p. 41
Donati J.-F., Semel M., Carter B. D., Rees D. E., Collier Cameron A., 1997, MNRAS, 291, 658
Donati J.-F., Kouach D., Lacombe M., Baratchart S., Doyon R., Delfosse X. et al., 2017, SPIRou: A nIR Spectropolarimeter/High-precision Velocimeter for the CFHT. Springer International Publishing AG, part of Springer Nature, p. 107
Dotter A., Chaboyer B., Jevremović D., Kostov V., Baron E., Ferguson J. W., 2008, ApJS, 178, 89
Dressing C. D., Charbonneau D., 2013, ApJ, 767, 95
Dressing C. D., Charbonneau D., 2015, ApJ, 807, 45
Freytag B., Steffen M., Ludwig H.-G., Wedemeyer-Böhm S., Schaffenberger W., Steiner O., 2012, J. Comput. Phys., 231, 919
Gaidos E., Fischer D. A., Mann A. W., Howard A. W., 2013, ApJ, 771, 18
Gough D. O., 1977, ApJ, 214, 196
Gray D. F., 1975, ApJ, 202, 148
Gray D. F., 2005, The Observation and Analysis of Stellar Photospheres. Cambridge University Press, United Kingdom
Gustafsson B., Edvardsson B., Eriksson K., Jørgensen U. G., Nordlund Å., Plez B., 2008, A&A, 486, 951
Heiter U., Jofré P., Gustafsson B., Korn A. J., Soubiran C., Thévenin F., 2015, A&A, 582, A49
Henry T. J., Jao W.-C., Subasavage J. P., Beaulieu T. D., Ianna P. A., Costa E., Méndez R. A., 2006, AJ, 132, 2360
Husser T.-O., Wende-von Berg S., Dreizler S., Homeier D., Reiners A., Barman T., Hauschildt P. H., 2013, A&A, 553, A6
Jofré P. et al., 2017, A&A, 601, A38

Kupka F., Piskunov N., Ryabchikova T. A., Stempels H. C., Weiss W. W., 1999, A&AS, 138, 119
Kupka F., Dubernet M.-L., VAMDC Collaboration, 2011, Baltic Astron., 20, 503
Kurucz R. L., 1979, ApJS, 40, 1
Kurucz R. L., Bell B., 1995, Atomic line list. Smithsonian Astrophysical Obervatory, Cambridge, MA
Levenberg K., 1944, Q. J. Appl. Math., 2, 164
Ligi R. et al., 2016, A&A, 586, A94
Lindegren L., Perryman M. A. C., 1996, A&AS, 116, 579
Ludwig H.-G., Freytag B., Steffen M., 1999, A&A, 346, 111
Magic Z. et al., 2013, A&A, 557, A26
Mann A. W., Brewer J. M., Gaidos E., Lépine S., Hilton E. J., 2013a, AJ, 145, 52
Mann A. W., Gaidos E., Ansdell M., 2013b, ApJ, 779, 188
Mann A. W., Deacon N. R., Gaidos E., Ansdell M., Brewer J. M., Liu M. C., Magnier E. A., Aller K. M., 2014, AJ, 147, 160
Mann A. W., Feiden G. A., Gaidos E., Boyajian T., von Braun K., 2015, ApJ, 804, 64
Marquardt D. W., 1963, J. Soc. Ind. Appl. Math., 11, 431
McKemmish L. K., Yurchenko S. N., Tennyson J., 2016, MNRAS, 463, 771
Morin J. et al., 2008, MNRAS, 390, 567
Morin J., 2012, in Reylé C., Charbonnel C., Schultheis M., eds, EAS Publications Series Vol. 57, EAS Publications Series, ESA Publication Series, p. 165
Muirhead P. S., Hamren K., Schlawin E., Rojas-Ayala B., Covey K. R., Lloyd J. P., 2012, ApJ, 750, L37
Neves V., Bonfils X., Santos N. C., Delfosse X., Forveille T., Allard F., Udry S., 2014, A&A, 568, A121
Newton E. R., Charbonneau D., Irwin J., Mann A. W., 2015, ApJ, 800, 85
Newton E. R., Irwin J., Charbonneau D., Berta-Thompson Z. K., Dittmann J. A., West A. A., 2016, ApJ, 821, 93
Petit P., Louge T., Théado S., Paletou F., Manset N., Morin J., Marsden S. C., Jeffers S. V., 2014, PASP, 126, 469
Piskunov N. E., Kupka F., Ryabchikova T. A., Weiss W. W., Jeffery C. S., 1995, A&AS, 112, 525
Prandtl L., 1925, Math. Mech. 5, 1, 136
Press W. H., Teukolsky S. A., Vetterling W. T., Flannery B. P., 1992, Numerical recipes in FORTRAN. The art of scientific computing. Cambridge University Press, United Kingdom
Quirrenbach A. et al., 2012, in Ground-based and Airborne Instrumentation for Astronomy IV, SPIE, p. 84460R
Rajpurohit A. S., Reylé C., Allard F., Scholz R.-D., Homeier D., Schultheis M., Bayo A., 2014, A&A, 564, A90
Rajpurohit A. S., Allard F., Teixeira G. D. C., Homeier D., Rajpurohit S., Mousis O., 2018a, A&A, 610, A19
Rajpurohit A. S., Allard F., Rajpurohit S., Sharma R., Teixeira G. D. C., Mousis O., Kamlesh R., 2018b, A&A, 620, A180
Rauer H. et al., 2014, Exp. Astron., 38, 249
Recio-Blanco A., Bijaoui A., de Laverny P., 2006, MNRAS, 370, 141
Ricker G. R., et al., 2014, in Space Telescopes and Instrumentation 2014: Optical, Infrared, and Millimeter Wave. SPIE, p. 914320
Santos N. C. et al., 2013, A&A, 556, A150
Schmidt M., 1963, ApJ, 137, 758
Schweitzer A., Hauschildt P. H., Allard F., 1996, in Pallavicini R., Dupree A. K., eds, Astronomical Society of the Pacific Conference Series Vol. 109, Cool Stars, Stellar Systems, and the Sun. San Francisco, CA 94112, p. 571
Stello D. et al., 2009, ApJ, 700, 1589
Takeda Y., UeNo S., 2017, PASJ, 69, 46
Takeda G., Ford E. B., Sills A., Rasio F. A., Fischer D. A., Valenti J. A., 2007, ApJS, 168, 297
Tinsley B. M., 1980, Fund. Cosmic Phys., 5, 287
Torres G., Fischer D. A., Sozzetti A., Buchhave L. A., Winn J. N., Holman M. J., Carter J. A., 2012, ApJ, 757, 161
Ulrich R. K., 1986, ApJ, 306, L37
Valenti J. A., Fischer D. A., 2005, ApJS, 159, 141
van den Bergh S., 1962, AJ, 67, 486
Wende S., Reiners A., Ludwig H.-G., 2009, A&A, 508, 1429
Woolf V. M., West A. A., 2012, MNRAS, 422, 1489
Worthey G., 1994, ApJS, 95, 107
Yıldız M., Çelik Orhan Z., Kayhan C., 2016, MNRAS, 462, 1577

APPENDIX A: ADDITIONAL FIGURES

Table A1. List of the lines that were modified. log gf is the initial oscillator strength, log gf_{corr} is the corrected one, σ_W is van der Waals damping parameter from VALD, and σ_{Wcorr} is the corrected van der Waals damping parameter. Only the corrected values of van der Waals damping parameter were used, if not PHOENIX internal approximation was used (Schweitzer et al. 1996) .

Elements	Wavelength (nm)	log gf	log gf_{corr}	σ_W	σ_{Wcorr}
Cr 2	523.39524	− 2.360	− 2.166	− 7.776	
Fe 1	523.43965	− 0.058	− 0.194	− 7.280	− 7.225
Fe 1	523.45229	− 4.675	− 6.675	− 7.820	
V 1	523.51488	− 0.530	− 0.977	− 7.560	
Ti 1	523.52677	− 2.859	− 3.026	− 7.800	
V 1	523.55298	0.110	− 0.075	− 7.616	
Nd 2	523.56472	− 0.510	− 0.567	0.000	
Fe 2	523.60799	− 2.230	− 2.433	− 7.880	− 7.349
Co 1	523.61773	− 1.254	− 0.252	− 7.510	
Co 1	523.66401	− 1.470	− 1.461	− 7.594	
Fe 1	523.68442	− 0.854	− 1.038	− 7.700	− 7.002
Ni 1	523.69544	− 0.947	− 1.105	− 7.510	
Fe 1	523.76593	− 1.497	− 1.647	− 7.710	
Fe 1	523.78378	− 2.430	− 2.174	− 7.179	
Fe 1	523.87217	− 3.451	− 2.944	− 7.820	
Cr 2	523.87865	− 1.350	− 1.351	− 7.776	− 7.154
Cr 1	523.92907	− 0.929	− 1.137	− 7.360	
Ti 1	523.99949	− 0.916	− 0.727	− 7.550	
Ti 1	524.00463	− 2.074	− 2.182	− 7.800	
Cr 1	524.04194	− 1.270	− 1.351	− 7.570	
Cr 1	524.19319	− 0.706	− 0.493	− 7.280	− 6.146
Sc 2	524.12717	− 0.765	− 0.780	− 7.830	
Fe 1	524.13723	− 1.750	− 1.513	− 7.110	− 5.666
V 1	524.23225	0.170	0.3199	− 7.615	− 6.686
Cr 1	524.29171	− 1.920	− 1.925	− 7.570	
Fe 1	524.33592	− 1.670	− 2.103	− 7.122	
Fe 1	524.39499	− 0.967	− 1.117	− 7.578	− 7.157
Fe 1	524.45390	− 2.474	− 4.484	− 7.120	
Cr 1	524.46025	− 1.238	− 0.556	− 7.380	
Cr 1	524.48136	− 0.537	− 0.618	− 7.262	
Fe 1	524.52355	− 0.842	− 1.676	− 7.510	
Ni 1	524.70679	− 2.508	− 0.518	− 7.560	
Fe 1	524.74531	− 2.275	− 3.721	− 7.800	
Ti 1	524.80108	− 2.355	− 2.357	− 7.800	
Ti 1	524.81036	− 0.893	− 1.569	− 7.770	
Cr 2	524.82285	− 2.466	− 2.358	− 7.862	
Fe 1	524.85104	− 4.946	− 4.850	− 7.822	− 7.737
Ti 1	524.87507	− 0.640	− 0.857	− 7.237	− 5.812
Cr 1	524.90257	− 1.590	− 1.602	− 7.621	− 7.619
Co 1	524.93808	− 2.070	− 2.037	− 7.652	
Ni 1	524.98291	− 2.076	− 2.233	− 7.500	
Ti 1	524.98447	− 1.680	− 1.362	− 7.630	
Ni 1	525.04907	− 2.728	− 1.329	− 7.500	
Cr 2	525.08982	− 2.489	− 2.364	− 7.859	
Nd 2	525.10413	0.200	0.4576	0.000	
Co 1	525.14623	− 1.047	− 0.228	− 7.520	
Fe 1	525.16703	− 4.938	− 4.849	− 7.820	
Fe 1	525.21069	− 2.181	− 2.258	− 7.602	− 7.133
Ti 1	525.23822	− 2.578	− 2.465	− 7.800	
Ti 1	525.29398	− 2.976	− 2.841	− 7.800	
Fe 1	525.34283	− 4.005	− 2.005	− 7.820	
Ti 1	525.35616	− 2.360	− 2.387	− 7.726	
Fe 1	525.44827	− 3.940	− 3.804	− 7.570	− 5.108
Fe 1	525.49240	− 1.573	− 1.689	− 7.203	− 7.148
Co 1	525.61106	− 0.239	− 0.302	− 7.510	
Cr 1	525.65768	− 0.100	− 0.207	− 7.540	− 6.550
Mn 1	525.67428	− 0.851	− 1.061	− 7.563	
Nd 2	525.69685	− 0.670	− 0.724	− 7.000	

Table A1 – *continued*

Elements	Wavelength (nm)	log gf	log gf_{corr}	σ_W	σ_{Wcorr}
Fe 1	525.71255	− 1.550	− 1.946	− 7.520	
Fe 1	525.71979	− 1.451	− 1.877	− 7.510	− 7.520
Ti 1	525.72729	− 0.610	− 0.747	− 7.550	
Fe 1	525.84560	− 2.158	− 1.841	− 7.120	
Fe 1	526.05575	− 0.706	− 2.525	− 7.510	
Ni 1	526.09353	− 2.272	− 1.891	− 7.510	
Pr 2	526.11919	0.114	− 0.341	− 7.567	− 7.577
Ti 1	526.14366	− 0.180	− 0.233	− 7.225	
Ti 1	526.14366	− 0.180	− 0.233	− 7.225	
Ni 1	600.89737	− 3.400	− 3.364	− 7.813	
Co 1	600.93409	− 0.603	− 0.391	− 7.450	
Fe 1	600.93900	− 2.502	− 1.686	− 7.540	
Fe 1	600.96233	− 0.597	− 0.672	− 7.510	− 7.298
Fe 1	601.02197	− 0.982	− 0.894	− 7.540	− 7.335
Fe 1	601.38746	− 4.038	− 3.876	− 7.649	− 6.892
Ti 1	601.44012	− 1.251	− 1.877	− 7.770	
Fe 1	601.44201	− 2.984	− 2.691	− 7.510	
Si 1	601.44385	− 2.130	− 3.692	− 6.720	
C 1	601.48328	− 1.314	− 2.086	− 7.090	
Ti 1	601.50819	− 2.720	− 2.106	− 7.627	
Mn 1	601.51755	− 0.352	− 0.090	− 7.560	− 7.487
Fe 1	601.77154	− 2.086	− 2.539	− 7.290	
V 1	601.77234	− 0.484	− 4.813	− 7.760	
Si 1	601.78762	− 1.645	− 4.813	− 6.970	
Fe 1	601.82710	− 1.820	− 1.965	− 7.797	− 7.233
Mn 1	601.83364	− 0.183	− 0.539	− 7.560	− 7.235
Fe 1	602.34799	− 0.760	− 0.707	− 7.540	− 7.276
Mn 1	602.34877	− 0.154	− 0.082	− 7.560	− 7.570
Fe 1	603.57057	− 2.420	− 2.271	− 7.279	
Si 1	602.38972	− 1.966	− 2.169	− 6.810	
Fe 1	602.57251	− 0.120	− 0.030	− 7.225	
Fe 1	602.87196	− 1.089	− 1.168	− 7.780	
Fe 1	602.89780	− 1.754	− 2.095	− 7.350	
Si 1	602.93823	− 1.648	− 2.052	− 6.660	
Fe 1	602.93924	− 2.125	− 4.290	− 7.290	
Ti 1	603.33405	− 4.008	− 4.250	− 7.770	
Fe 1	603.43406	− 3.330	− 3.188	− 7.540	
Fe 1	603.70079	− 2.590	− 2.466	− 7.502	
Si 1	603.87505	− 1.469	− 4.660	− 6.660	
V 1	604.13981	− 0.650	− 0.661	− 7.613	− 7.872
Fe 1	604.31377	− 1.500	− 4.340	− 7.340	
Fe 1	604.36235	− 1.303	− 4.330	− 7.330	
Si 1	604.40720	− 1.316	− 4.720	− 6.720	
S 1	604.76465	− 1.318	− 0.528	− 7.020	
S 1	604.77123	− 1.114	− 0.670	− 7.020	
Si 1	604.83678	− 0.936	− 6.690	− 6.690	
Fe 1	604.87319	− 2.024	− 6.290	− 7.290	
Si 1	604.91903	− 1.246	− 6.660	− 6.660	
Si 1	604.91428	− 2.016	− 6.000	− 7.000	
S 1	605.43319	− 0.829	− 0.450	− 7.020	
Cr 2	605.51422	− 2.229	− 2.102	− 7.831	− 7.841
Ni 1	605.53614	− 1.070	− 0.972	− 7.227	− 7.333
Fe 1	605.57493	− 2.310	− 2.188	− 7.270	− 7.025
Fe 1	605.67661	− 2.174	− 2.009	− 7.320	
Fe 1	605.70783	− 1.479	− 2.252	− 7.330	
Fe 1	605.76811	− 0.460	− 0.447	− 7.130	− 7.134
Fe 1	605.89301	− 1.344	− 1.800	− 7.330	
Fe 1	605.92025	− 1.843	− 3.500	− 7.330	
V 1	605.98195	− 1.400	− 1.667	− 7.618	
Fe 1	606.22388	− 1.394	− 8.340	− 7.340	
Fe 1	606.33199	− 2.233	− 2.180	− 7.320	− 7.330
Cr 1	606.43527	− 1.588	− 1.505	− 7.520	− 7.530

Table A1 *– continued*

Elements	Wavelength (nm)	log gf	log gf_{corr}	σ_W	σ_{Wcorr}
Fe 1	606.45259	− 4.140	− 3.993	− 7.691	− 8.821
Fe 1	606.46223	− 1.482	− 2.237	− 7.310	
Fe 1	606.49865	− 0.862	− 6.351	− 7.350	
Si 1	606.56722	− 2.844	− 2.275	− 6.790	
Ti 1	606.63054	− 1.944	− 1.865	− 7.733	− 7.329
Fe 1	606.71608	− 1.530	− 1.547	− 7.584	− 7.594
Si 1	610.26228	− 2.078	− 6.680	− 6.680	
Fe 1	610.38558	− 0.544	− 1.909	− 7.510	
Fe 1	610.38602	− 0.517	− 0.369	− 7.410	− 6.791
Ca 1	610.44124	− 0.793	− 0.626	− 7.189	− 7.481
Fe 1	610.48742	− 0.630	− 0.642	− 7.420	− 6.725
Fe 1	610.49826	− 1.117	− 1.258	− 7.510	− 6.925
Si 1	610.57084	− 1.946	− 6.680	− 6.680	
Fe 1	610.62464	− 2.038	− 6.320	− 7.320	
Fe 1	610.68173	− 2.050	− 1.997	− 7.243	
Si 1	610.82982	− 1.897	− 2.068	− 7.120	
Fe 1	610.90139	− 1.577	− 6.790	− 7.790	
Ni 1	610.98068	− 2.600	− 2.538	− 7.705	− 7.717
Ni 1	611.27620	− 0.870	− 0.797	− 7.214	− 6.562
V 1	611.33424	− 0.740	− 0.856	− 7.620	
Si 1	611.46200	− 1.956	− 2.090	− 7.120	
Fe 2	611.50115	− 4.110	− 4.185	− 7.893	− 7.903
Ni 1	611.78727	− 0.529	− 0.426	− 7.500	− 6.481
Ni 1	611.78738	− 1.080	− 3.084	− 7.500	− 7.510
Co 1	611.86835	− 2.490	− 2.718	− 7.721	
V 1	612.12214	− 0.360	− 0.326	− 7.618	
Ni 1	612.14507	− 1.350	− 1.283	− 7.238	− 7.248
Ti 1	612.26962	− 1.420	− 1.663	− 7.670	
Ca 1	612.39117	− 0.316	− 0.044	− 7.189	− 7.521
Si 1	612.67163	− 1.465	− 1.427	− 7.130	
Ti 1	612.79117	− 1.425	− 1.400	− 7.733	
Si 1	612.83011	− 2.489	− 6.660	− 6.660	
Fe 1	612.96020	− 1.399	− 1.467	− 7.790	
Fe 1	612.98161	− 1.958	− 2.141	− 7.320	
Ni 1	613.06697	− 3.430	− 3.352	− 7.816	
Ni 1	613.18316	− 0.960	− 0.907	− 7.225	− 7.235
Si 1	613.32701	− 1.557	− 1.570	− 7.130	− 6.205
Si 1	613.35488	− 1.617	− 1.633	− 7.130	− 6.975
Cr 1	613.74804	− 0.071	− 0.276	− 7.540	
Fe 1	613.74846	− 1.857	− 1.533	− 7.320	
Fe 1	613.83130	− 1.400	− 1.453	− 7.609	− 7.577
Fe 1	613.86921	− 2.950	− 2.933	− 7.691	− 7.810
Fe 1	613.91967	− 2.512	− 3.263	− 7.580	− 8.590
Fe 1	613.93897	− 1.403	− 1.293	− 7.589	− 7.718
Si 1	614.67167	− 1.311	− 1.334	− 7.130	
Ti 1	614.79079	− 1.480	− 1.757	− 7.670	
Co 1	614.81048	− 2.973		− 7.810	
Fe 1	614.81135	− 2.082	− 5.300	− 7.300	
Si 1	614.84140	− 2.228	− 5.730	− 6.730	
Fe 2	614.94356	− 2.827	− 2.832	− 7.870	
Fe 1	614.95354	− 1.671	− 1.619	− 7.800	− 8.006
Fe 2	615.09478	− 2.720	− 2.783	− 7.870	
Ti 1	615.14265	− 1.440	− 1.634	− 7.770	
Fe 2	615.17969	− 4.817	− 4.580	− 7.892	
V 1	615.18586	− 1.780	− 1.805	− 7.738	− 8.357
Fe 1	615.33194	− 3.299	− 3.302	− 7.696	− 7.706
Si 1	615.39950	− 1.358	− 5.660	− 6.660	
Na 1	615.59287	− 1.547	− 1.527	0.000	
Si 1	615.68378	− 0.755	− 0.736	− 7.130	
Fe 1	615.80746	− 3.274	− 3.711	− 7.580	
Fe 1	615.85080	− 1.495	− 2.223	− 7.340	

Table A1 *– continued*

Elements	Wavelength (nm)	log gf	log gf_{corr}	σ_W	σ_{Wcorr}
Fe 1	615.94317	− 1.260	− 1.266	− 7.790	− 7.071
Fe 1	616.10776	− 2.373	− 2.485	− 7.510	
Cr 1	616.11286	− 1.705	− 3.664	− 7.380	
Ca 1	616.30021	− 1.266	− 1.242	− 7.145	− 7.415
Ca 1	616.38784	− 0.090	0.318	− 7.189	− 7.690
Ni 1	616.51297	− 0.653	− 0.799	− 7.510	
Fe 1	616.52490	− 3.619	− 3.628	− 7.661	
Ca 1	616.54608	− 1.286	− 1.194	− 7.146	− 8.624
Fe 1	616.62523	− 1.204	− 5.500	− 7.500	
Fe 1	616.70657	− 1.474	− 1.478	− 7.780	− 7.721
Ca 1	616.81455	− 1.142	− 1.122	− 7.146	− 7.156
Fe 1	616.95658	− 1.922	− 2.339	− 7.780	
Ca 1	617.07492	− 0.797	− 0.689	− 7.146	− 7.298
Ca 1	617.12704	− 0.478	− 0.352	− 7.145	− 7.347
Fe 1	617.22131	− 0.440	− 0.501	− 7.119	− 6.816
Fe 1	617.25438	− 1.704	− 1.940	− 7.320	− 7.330
Fe 1	617.27168	− 1.985	− 4.510	− 7.510	
Fe 1	617.50423	− 2.880	− 3.000	− 7.690	− 7.048
Ni 1	617.85208	− 0.260	− 0.319	− 7.225	− 7.235
Ni 1	617.89510	− 3.460	− 3.716	− 7.760	
Si 1	631.29854	− 2.504	− 1.708	− 6.800	
Fe 1	631.32445	− 3.141	− 3.112	− 7.599	
Ni 1	631.64048	− 1.770	− 2.400	− 7.671	
Ni 1	631.64127	− 0.530	− 0.465	− 7.510	− 7.520
Fe 1	631.67239	− 1.565	− 1.819	− 7.320	
Fe 1	631.70520	− 1.232	− 1.337	− 7.790	− 7.778
Fe 1	631.71577	− 1.941	− 2.084	− 7.800	− 6.383
Fe 1	631.75572	− 1.710	− 1.682	− 7.800	− 7.810
Fe 1	631.97647	− 2.262	− 2.133	− 7.790	− 7.384
Ca 1	631.98557	0.510	− 0.840	− 7.500	− 7.510
Mg 1	632.04644	− 2.103	− 1.987	− 7.500	− 7.110
Mg 1	632.09845	− 2.324	− 2.164	− 7.542	− 6.187
C 1	658.05908	− 1.378	− 4.378	− 6.960	
Si 1	658.17732	− 1.929	− 3.150	− 7.130	
Ni 1	658.20310	− 1.261	− 1.073	− 7.500	− 6.083
Cr 1	658.27409	− 4.328	− 4.492	− 7.790	
Fe 1	658.30267	− 4.679	− 4.708	− 7.730	− 7.740
Si 1	658.55260	− 1.741	− 1.411	− 6.900	− 6.116
Ti 1	658.62390	− 0.090	− 0.266	− 7.530	− 7.540
Fe 1	658.63930	− 1.698	− 4.698	− 7.400	
Ni 1	658.81292	− 2.780	− 2.814	− 7.681	− 7.148
Fe 2	658.85276	− 2.849	− 2.838	− 7.763	
C 1	658.94297	− 1.003	− 1.085	− 7.260	
Si 1	658.99986	− 1.989	− 3.013	− 7.130	
Fe 1	659.31330	− 2.070	− 2.001	− 7.697	
Ni 1	659.43282	− 0.975	− 0.995	− 7.500	
Fe 1	659.44291	− 1.259	− 3.701	− 7.310	
Fe 1	659.47331	− 1.473	− 1.634	− 7.633	− 7.535
Si 1	659.48649	− 1.257	− 3.453	− 6.660	
Fe 1	659.56904	− 2.422	− 2.358	− 7.629	− 7.801
Co 1	659.76861	− 0.549	− 0.882	− 7.550	
Ti 1	659.83557	0.100	− 1.752	− 7.540	
Fe 1	659.93811	− 0.846	− 1.018	− 7.520	
Fe 1	659.93834	− 1.070	− 1.510	− 7.190	
Ni 1	660.04204	− 0.980	− 0.873	− 7.218	− 7.324
Ti 1	660.09276	− 2.085	− 2.086	− 7.667	
Fe 1	668.40818	− 2.851	− 5.310	− 7.810	
Fe 1	668.93368	− 2.524	− 3.824	− 7.820	
Fe 1	669.41188	− 2.396	− 3.100	− 7.810	
Fe 1	669.63942	− 1.269	− 2.672	− 7.310	
Al 1	669.78718	− 1.347	− 1.517	− 7.800	− 7.168

Table A1 – *continued*

Elements	Wavelength (nm)	log gf	log gf_{corr}	σ_W	σ_{Wcorr}
Fe 1	669.81641	– 0.670	– 1.557	– 7.185	– 7.429
Al 1	669.86370	– 1.421	– 0.742	0.000	
Al 1	669.86370	– 2.722	– 4.043	0.000	
Al 1	670.05225	– 1.647	– 1.821	– 7.800	– 6.773
Fe 1	670.09905	– 2.101	– 2.089	– 7.667	– 7.994
Fe 1	670.54164	– 3.160	– 3.031	– 7.633	– 8.523
Fe 1	670.63301	– 2.660	– 2.639	– 7.540	– 7.696
Fe 1	670.69517	– 1.382	– 1.068	– 7.480	– 7.360
Fe 1	671.01340	– 1.272	– 5.310	– 7.310	
Fe 1	671.09099	– 1.928	– 5.310	– 7.310	
Fe 1	671.21703	– 4.880	– 4.808	– 7.733	
Ni 1	671.34320	– 3.991	– 6.500	– 7.800	
Fe 1	671.36722	– 0.875	– 3.000	– 7.310	
Fe 1	671.43583	– 1.081	– 5.500	– 7.500	
Fe 1	671.45269	– 3.796	– 5.780	– 7.780	
Fe 1	671.48989	– 0.960	– 1.502	– 7.530	– 7.540
Fe 1	671.50481	– 2.972	– 2.480	– 7.700	
Fe 1	671.55956	– 1.600	– 1.437	– 7.207	– 7.217
Fe 1	671.72354	– 1.640	– 1.524	– 7.237	
Fe 1	671.80901	– 1.920	– 1.843	– 7.700	
Fe 1	671.93798	– 2.751	– 1.751	– 7.570	
Ti 1	744.26261	– 0.860	– 0.980	– 7.533	
Fe 1	744.29605	– 0.573	– 0.640	– 7.520	– 7.347
Fe 1	744.38459	– 2.116	– 2.374	– 7.520	– 7.530
Fe 1	744.50717	– 1.820	– 1.699	– 7.810	
Fe 1	744.52979	– 1.930	– 1.900	– 7.174	
Fe 1	744.77993	– 0.102	– 0.356	– 7.550	– 6.885
Fe 1	744.81061	– 1.144	– 2.076	– 7.260	
Fe 1	744.94443	– 0.846	– 0.978	– 7.510	– 7.530
Ca 1	745.03090	– 1.918	– 1.850	– 7.070	
Fe 2	745.13810	– 3.090	– 3.360	– 7.875	
Ca 1	745.25866	– 2.138	– 1.656	– 7.070	
Ca 1	745.36893	– 2.615	– 2.884	– 7.070	
Fe 1	745.41488	– 1.850	– 1.725	– 7.520	
Fe 1	745.49062	– 1.606	– 5.470	– 7.470	
Fe 1	745.60496	– 2.410	– 2.482	– 7.750	
Fe 1	745.68641	– 2.006	– 4.490	– 7.490	
Fe 1	745.68713	– 1.375	– 4.260	– 7.260	
Si 1	745.74291	– 2.404	– 1.835	– 7.060	
Co 1	745.93905	– 0.055	– 1.126	– 7.550	
Fe 1	746.35744	– 3.580	– 3.453	– 7.632	
Cr 1	746.43642	0.062	0.1230	– 7.530	
Fe 2	746.44652	– 2.871	– 2.982	– 7.875	
Fe 1	746.54377	– 1.720	– 1.574	– 7.185	
Fe 1	746.63490	– 1.066	– 1.235	– 7.260	
Fe 1	746.72895	– 1.017	– 5.260	– 7.260	
Fe 1	746.85778	– 3.295	– 4.526	– 7.480	
Fe 1	747.00853	– 1.932	– 5.360	– 7.360	
K 1	770.10834	– 0.154	– 1.170	– 7.445	
K 1	770.10834	– 0.154	– 1.170	– 7.445	
O 1	777.40828	0.369	0.538	– 7.469	
O 1	777.63054	0.223	0.356	– 7.469	
O 1	777.75277	0.002	0.109	– 7.469	
Fe 1	778.26971	0.030	– 0.029	– 7.540	– 7.242
Ca 1	778.90744	– 1.088	– 3.231	– 6.930	– 6.940
Ca 1	778.92503	– 0.343	– 1.272	– 6.930	
Ni 1	779.10735	– 2.180	– 1.857	– 7.728	– 7.738
Fe 1	779.63141	– 0.573	– 1.587	– 7.540	
Ni 1	779.97255	– 0.185	– 0.221	– 7.560	
Si 1	780.13258	– 0.655	– 1.405	– 6.980	

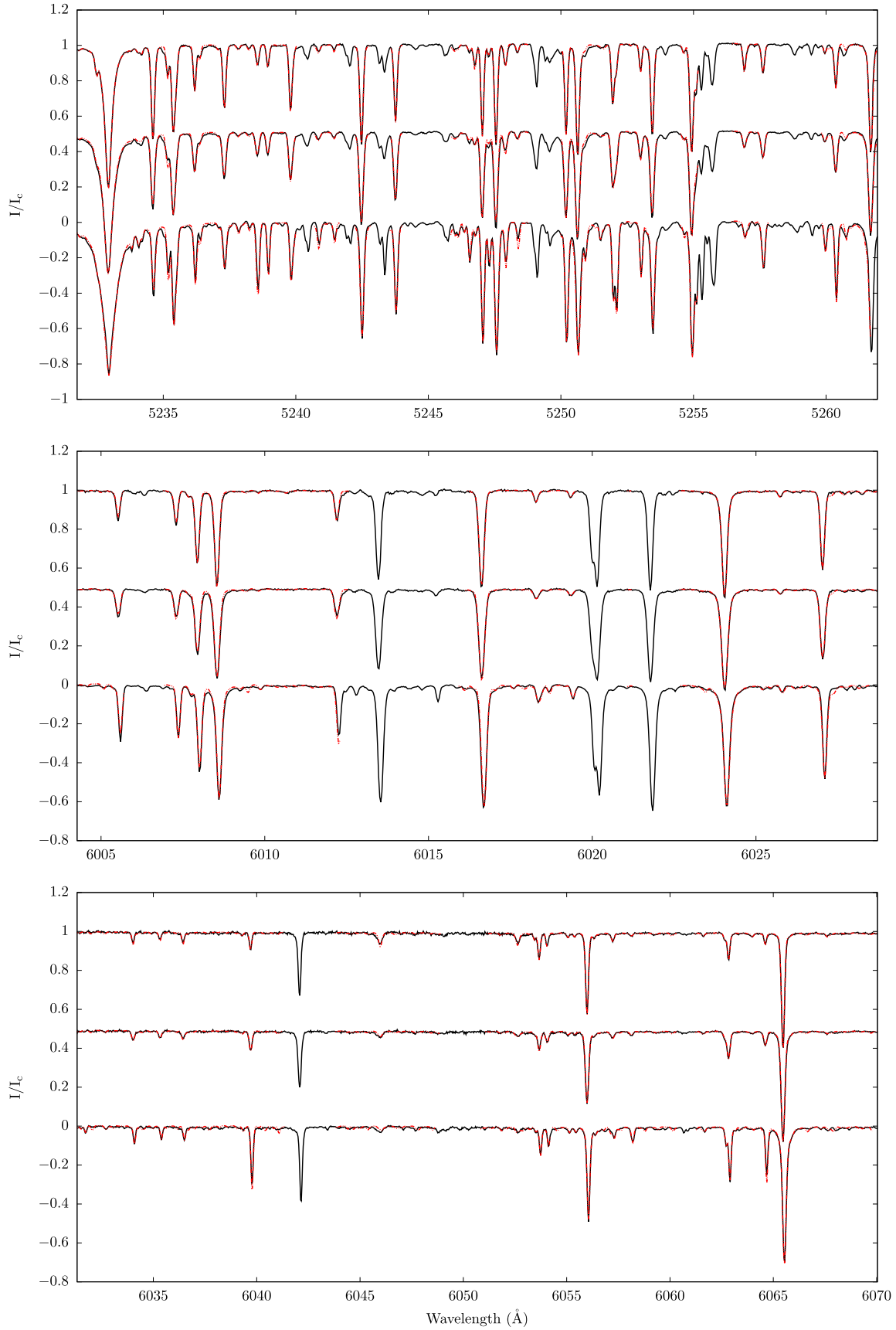

Figure A1. Synthetic (red) against observed (black) spectrum post calibrations in all used windows. From top to bottom, we have the Sun, ξ Boo A, and ϵ Eri.

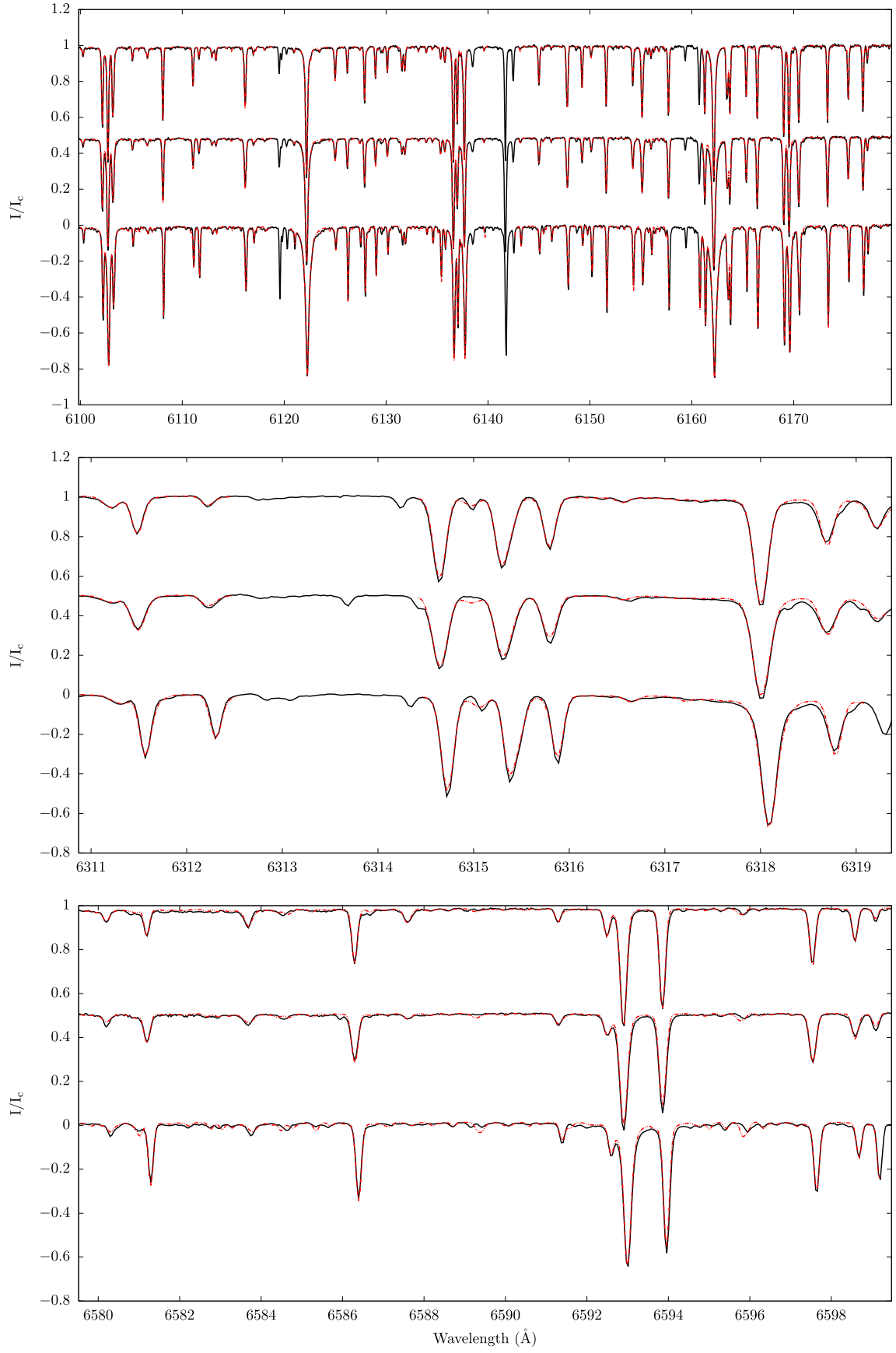

Figure A2. Synthetic (red) against observed (black) spectrum post calibrations in all used windows. From top to bottom we have the Sun, ξ Boo A and ϵ Eri.

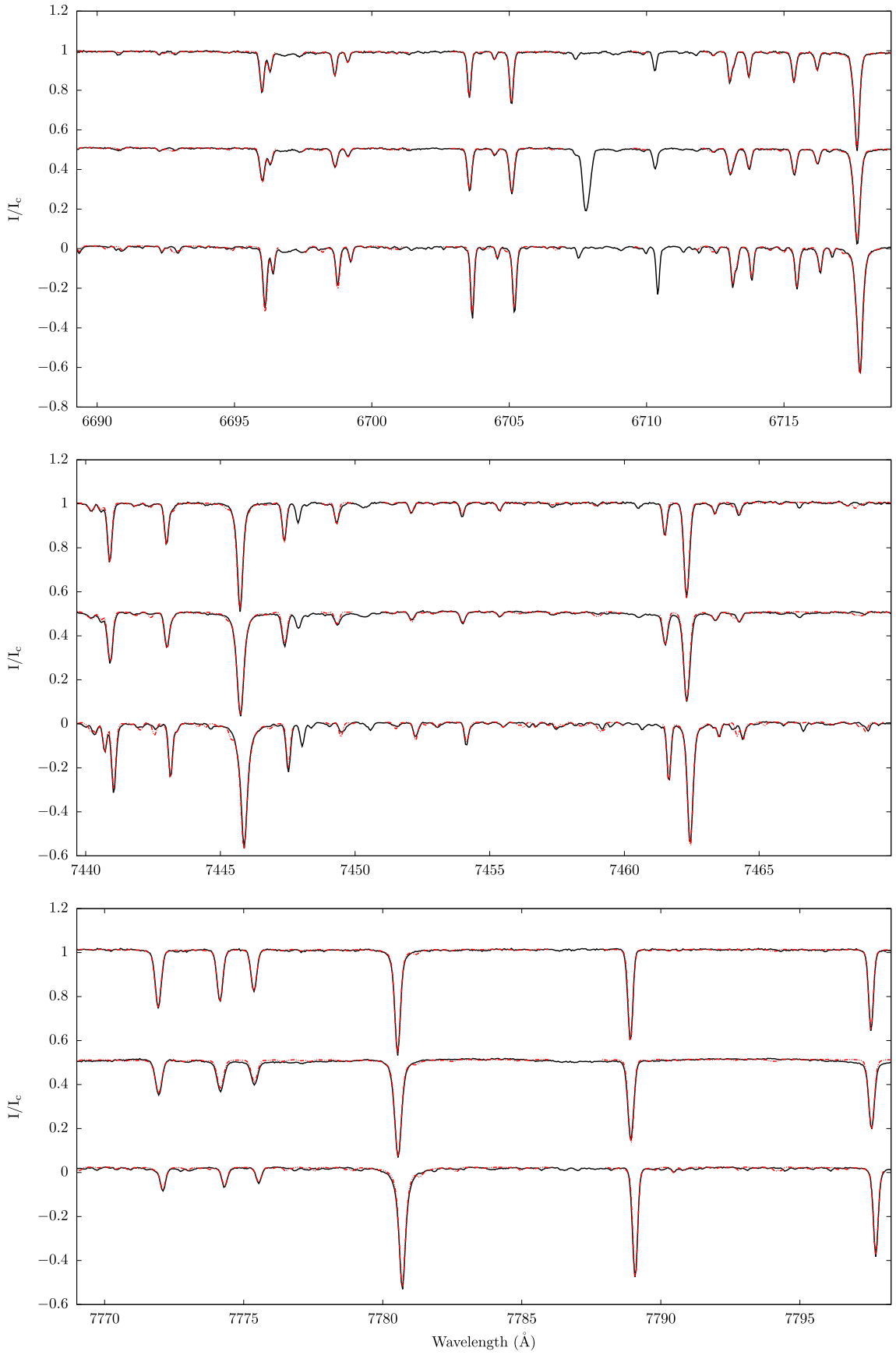

Figure A3. Synthetic (red) against observed (black) spectrum post calibrations in all used windows. From top to bottom, we have the Sun, ξ Boo A, and ϵ Eri.

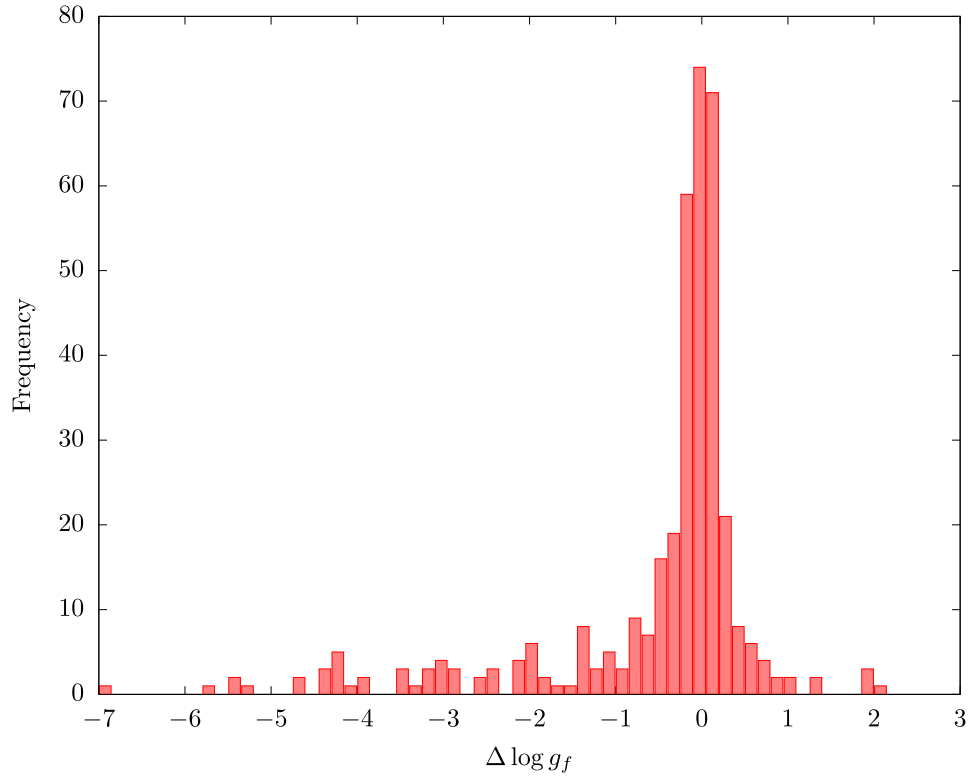

Figure A4. Histogram of $\Delta \log g_f$, the difference between the corrected $\log g_f$ and the uncorrected one . The larger tail in the negatives is due non-existent lines in the observed spectrum that were set to negative values in order to remove them from synthetic spectra. The standard deviation is 1.27, with a mean value of –0.50 for a total of 374.

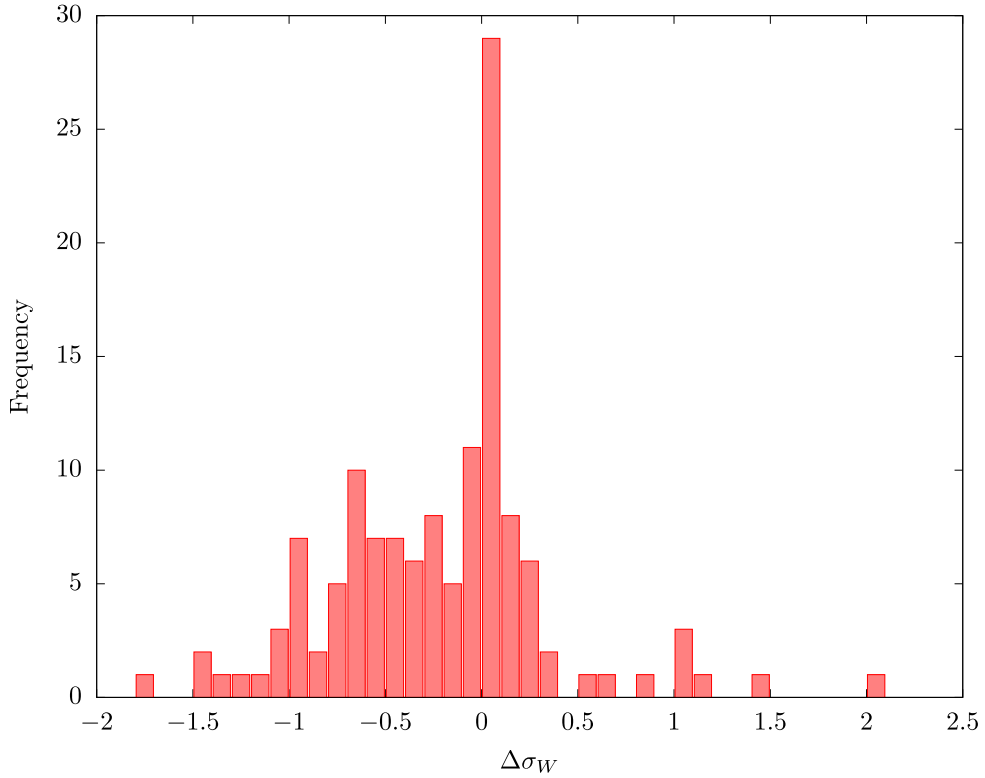

Figure A5. Histogram of $\Delta \sigma_W$, the difference between the corrected σ_W and the uncorrected one. The standard deviation is 0.56, with a mean value of –0.22, for a total of 131 lines.

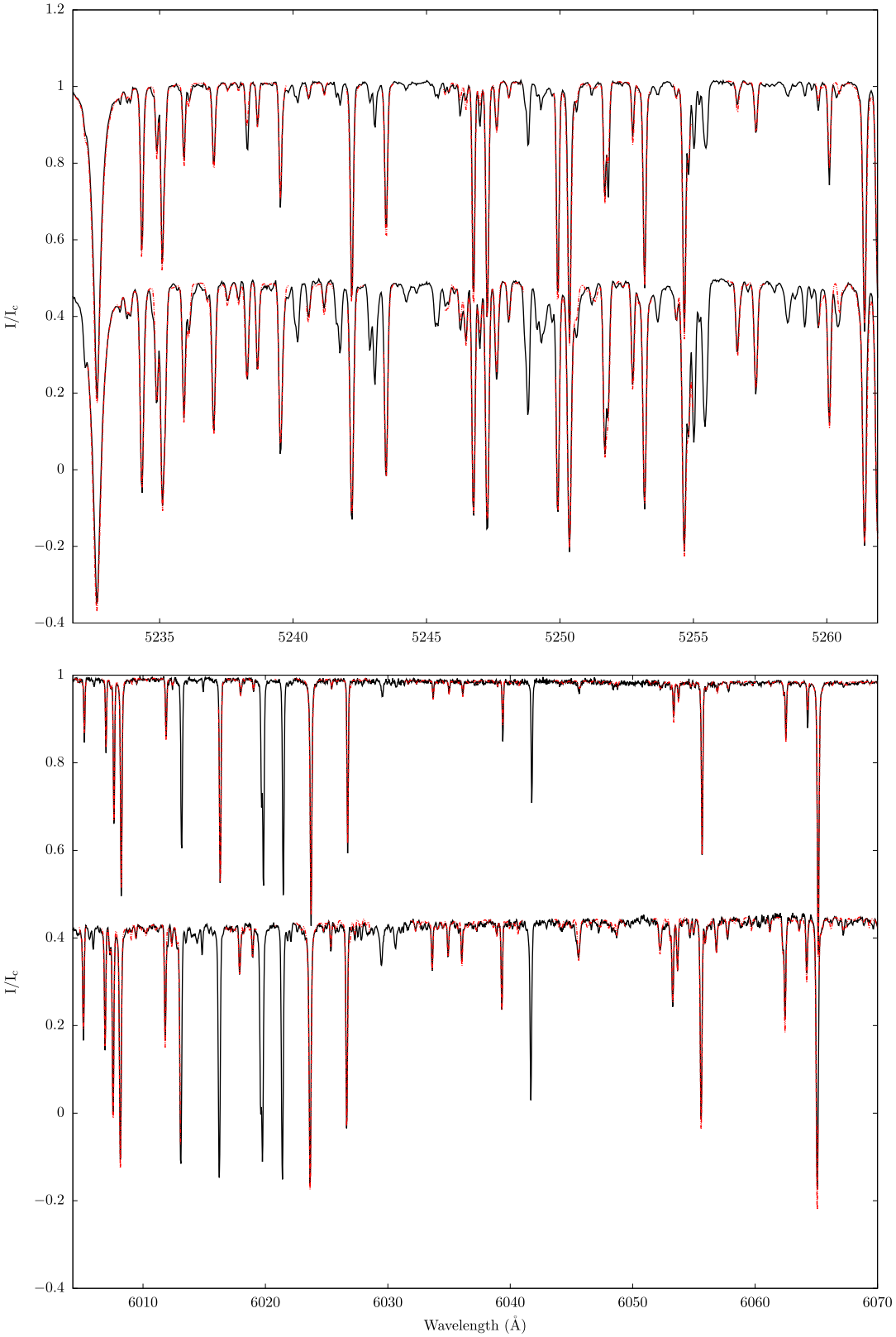

Figure A6. Synthetic (red) against observed (black) spectra post calibrations of τ Ceti (top) and HD 9540 (bottom). The HD 190360 spectra have been shifted downwards for these plots.

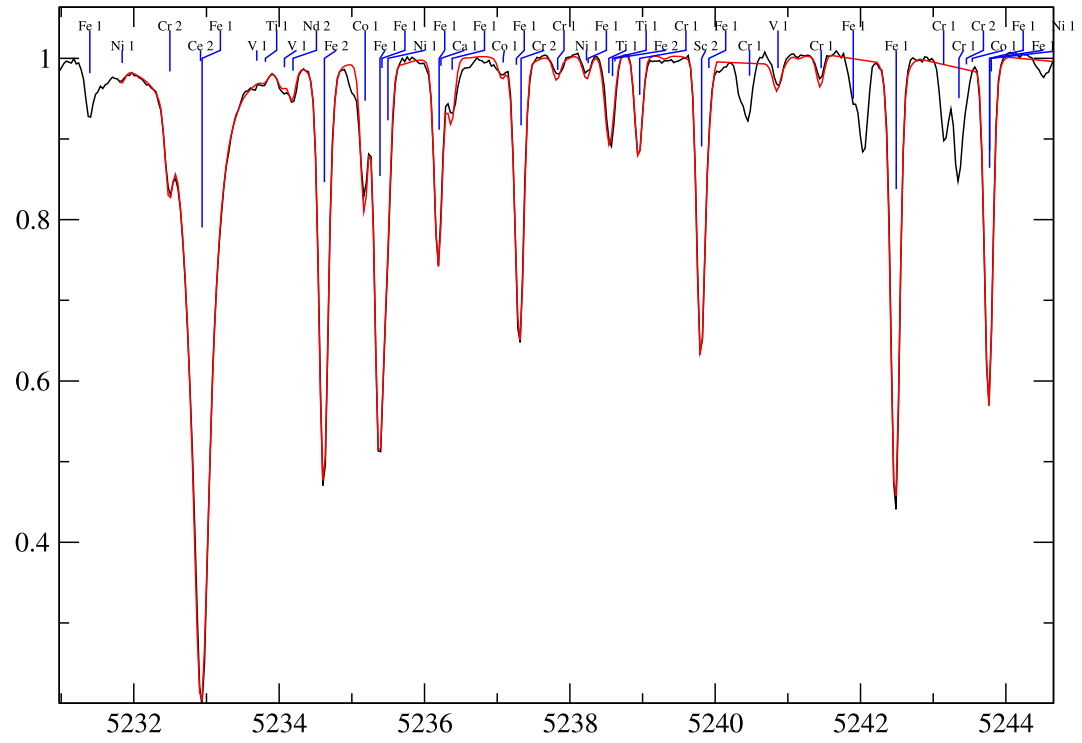

Figure A7. Synthetic (red) against observed (black) spectrum of the Sun post calibrations in all used windows with identified lines.

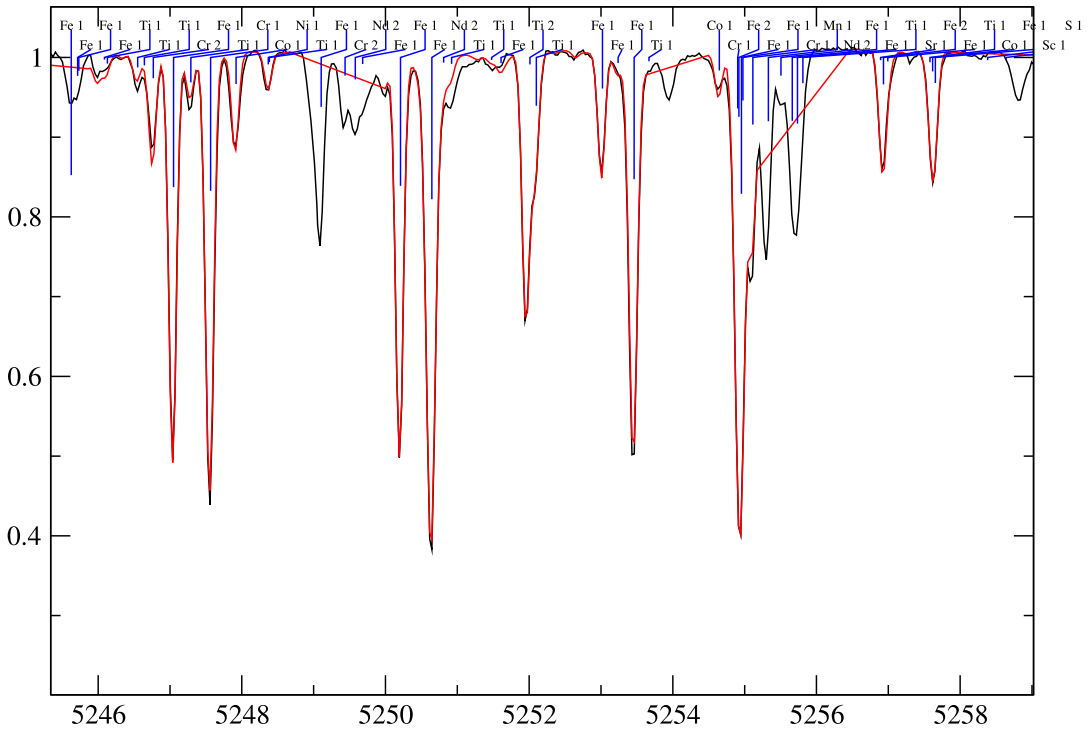

Figure A8. Synthetic (red) against observed (black) spectrum of the Sun post calibrations in all used windows with identified lines.

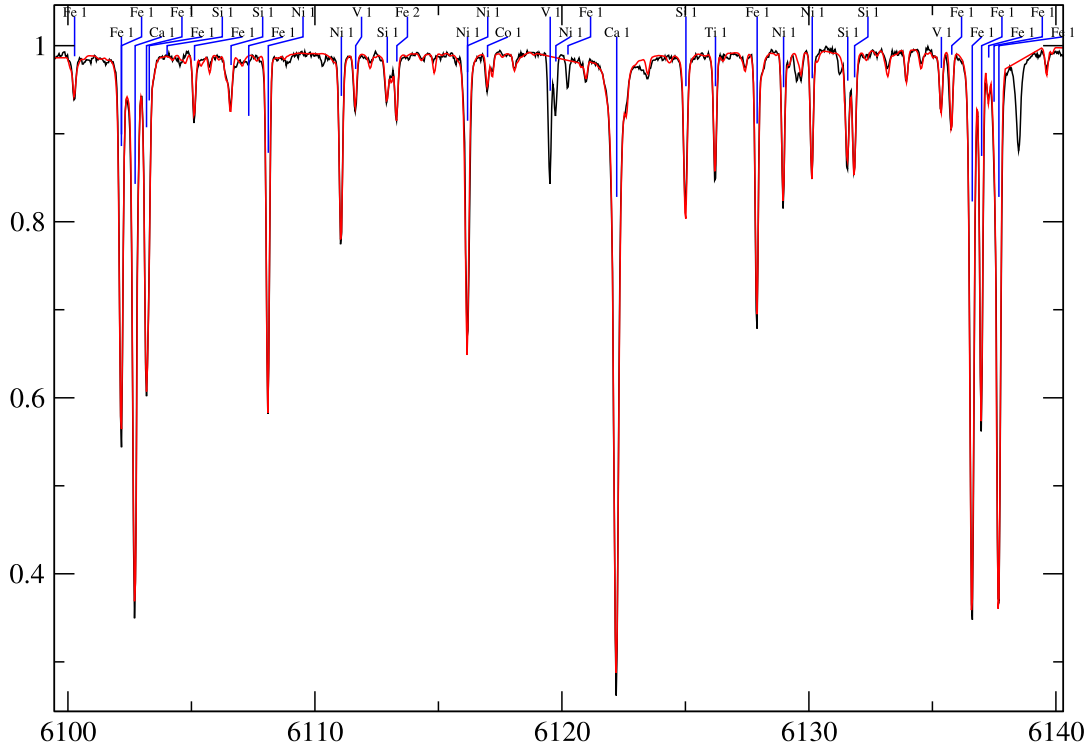

Figure A9. Synthetic (red) against observed (black) spectrum of the Sun post calibrations in all used windows with identified lines.

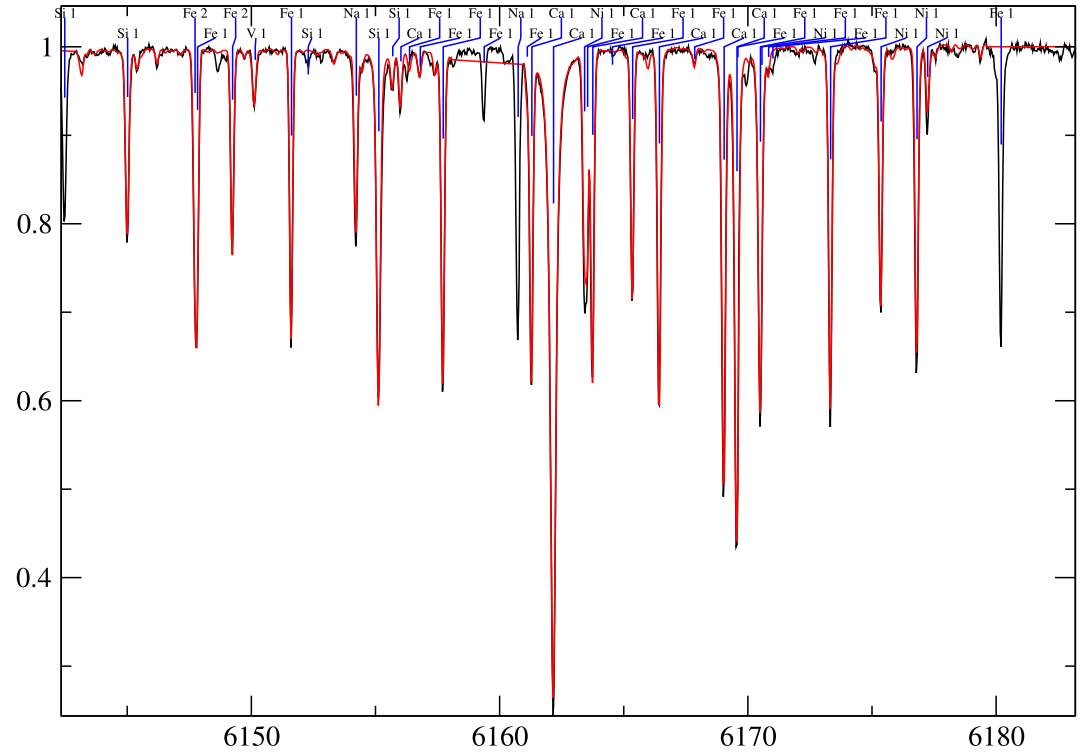

Figure A10. Synthetic (red) against observed (black) spectrum of the Sun post calibrations in all used windows with identified lines.

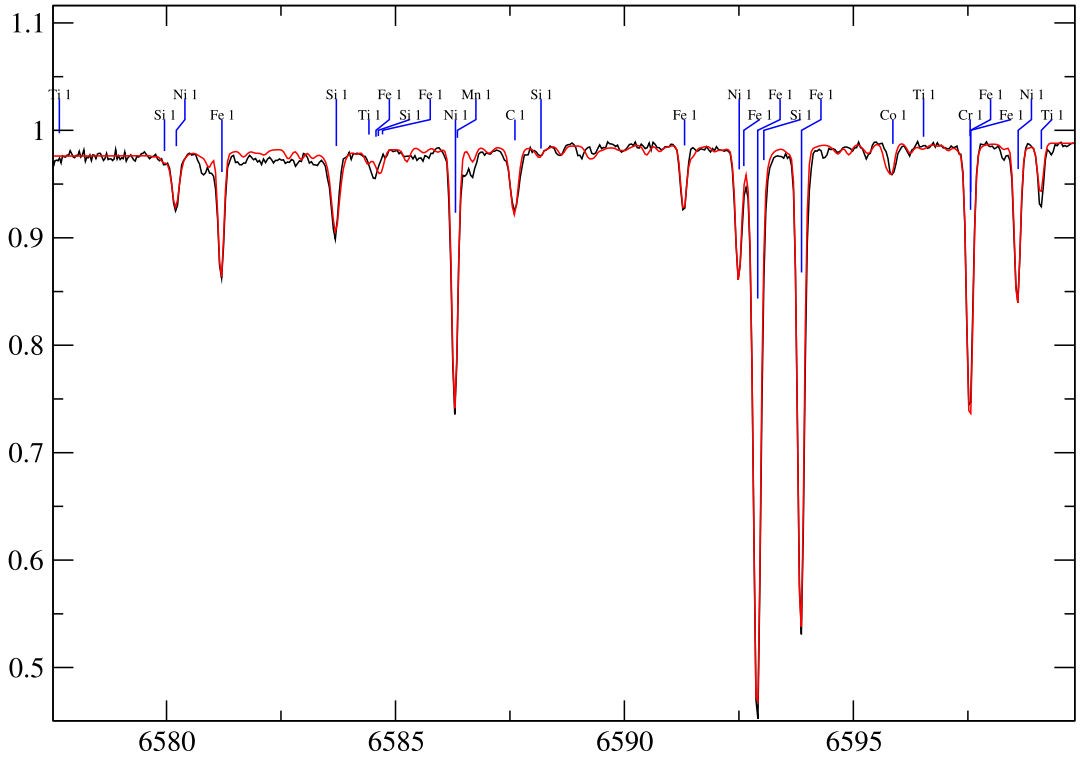

Figure A11. Synthetic (red) against observed (black) spectrum of the Sun post calibrations in all used windows with identified lines.

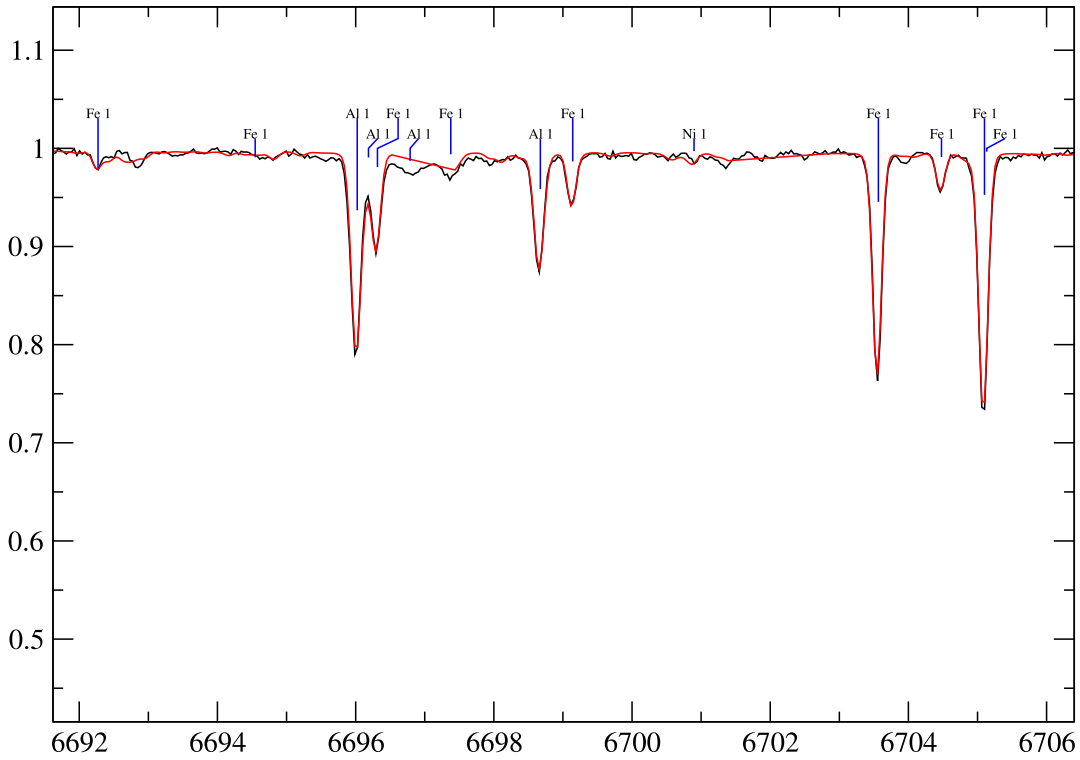

Figure A12. Synthetic (red) against observed (black) spectrum of the Sun post calibrations in all used windows with identified lines.

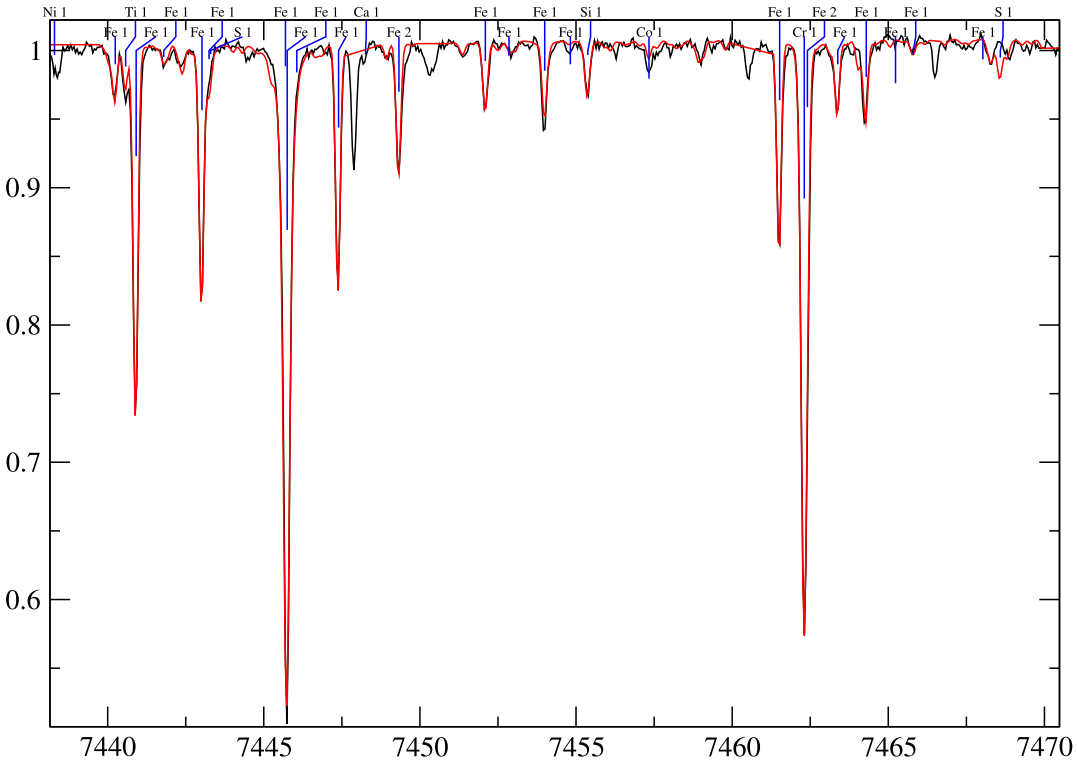

Figure A13. Synthetic (red) against observed (black) spectrum of the Sun post calibrations in all used windows with identified lines.

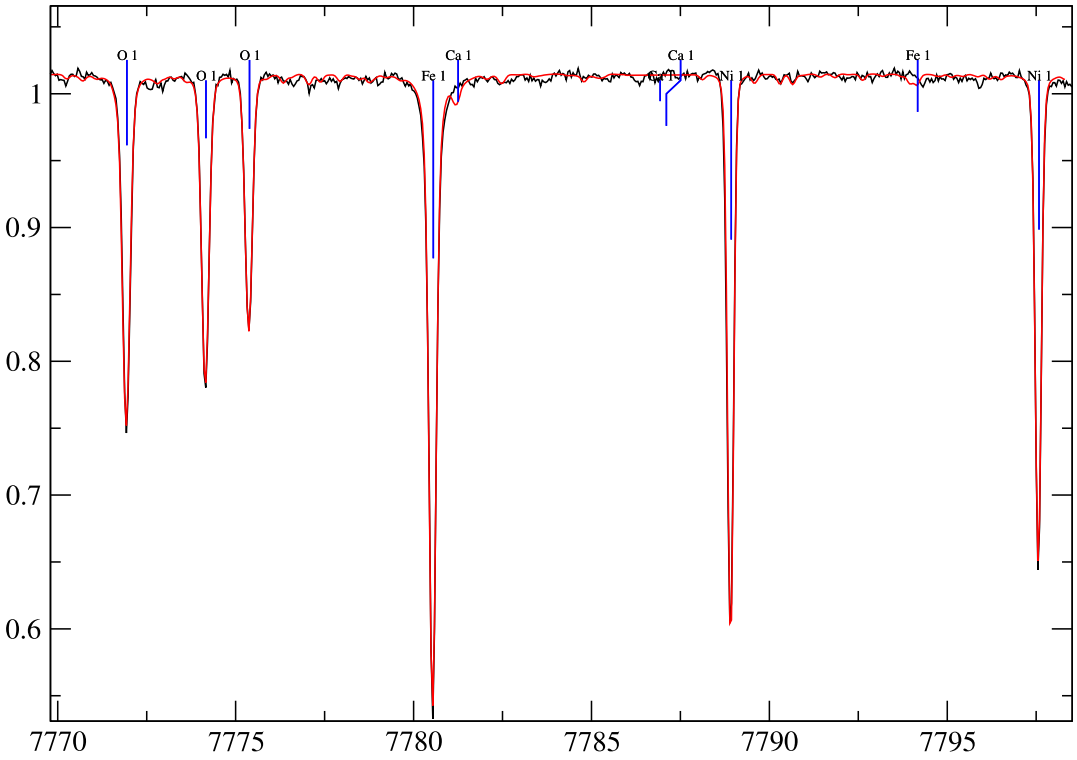

Figure A14. Synthetic (red) against observed (black) spectrum of the Sun post calibrations in all used windows with identified lines.

This paper has been typeset from a TEX/LATEX file prepared by the author.